Phosphonate Chelators for Medicinal Metal Ions

Thomas I. Kostelnik, Hayden Scheiber, Rosita Cappai, Neha Choudhary, Felix Lindheimer, María de Guadalupe Jaraquemada-Peláez,* and Chris Orvig*

Read Online

ACCESS | Metrics & More | Article Recommendations | SI Supporting Information

ABSTRACT: A family of phosphonate-bearing chelators was synthesized to study their potential in metal-based (radio)-pharmaceuticals. Three ligands (H_6phospa, H_6dipedpa, H_6eppy; structures illustrated in manuscript) were fully characterized, including X-ray crystallographic structures of H_6phospa and H_6dipedpa. NMR spectroscopy techniques were used to confirm the complexation of each ligand with selected trivalent metal ions. These methods were particularly useful in discerning structural information for Sc^{3+} and La^{3+} complexes. Solution studies were conducted to evaluate the complex stability of 15 metal complexes. As a general trend, H_6phospa was noted to form the most stable complexes, and H_6eppy associated with the least stable complexes.

Moreover, In^{3+} complexes were determined to be the most stable, and complexes with La^{3+} were the least stable, across all metals. Density functional theory (DFT) was employed to calculate structures of H_6phospa and H_6dipedpa complexes with La^{3+} and Sc^{3+}. A comparison of experimental ^1H NMR spectra with calculated ^1H NMR spectra using DFT-optimized structures was used as a method of structure validation. It was noted that theoretical NMR spectra were very sensitive to a number of variables, such as ligand configuration, protonation state, and the number/orientation of explicit water molecules. In general, the inclusion of an explicit second shell of water molecules qualitatively improved the agreement between theoretical and experimental NMR spectra versus a polarizable continuum solvent model alone. Formation constants were also calculated from DFT results using potential-energy optimized structures. Strong dependence of molecular free energies on explicit water molecule number, water molecule configuration, and protonation state was observed, highlighting the need for dynamic data in accurate first-principles calculations of metal−ligand stability constants.
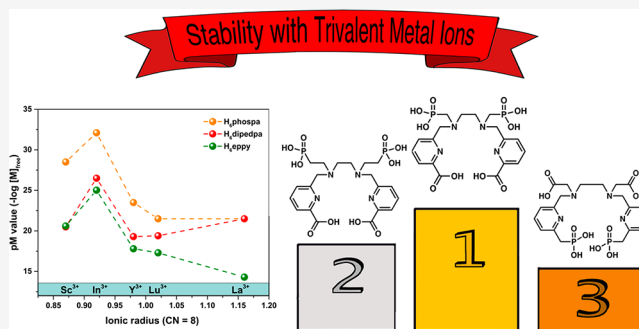
INTRODUCTION

Chelators have a wide range of utility due to the powerful repercussions of metal coordination. Many common applications of chelators capitalize on the biocompatible nature of these species by using them to securely deliver, release, or uptake metal ions within the human body. For example, nuclear medicine is a fast-growing field that has seen much success as a result of the development of metal-based radiopharmaceuticals.[1,2] Bifunctional chelators (BFCs) are often key components of contemporary metallo-radiopharmaceuticals, as they prevent the release of free radionuclides in vivo by maintaining a high thermodynamic stability and kinetic inertness to ensure the secure delivery of radioactive cargo.[1,2] Magnetic resonance imaging (MRI) contrast agents similarly require the metal complex to remain intact for an optimal performance. Unlike radiopharmaceuticals, however, MRI detects the T_1 relaxation of water within magnetic fields, and so these contrast agents aim to deliver metal ions capable of increasing the water relaxation rate at specific sites (e.g., the brain), often as a result of water coordination to a noncoordinatively saturated highly paramagnetic metal ion (e.g., Gd^{3+}, $Mn^{2+/3+}$, Cu^{2+}).[3] While these applications

necessitate the delivery of metal ions without their release, delivery and release of metal ions can be achieved through the rational tuning of chelators. This can be particularly useful when metal ion incorporation into tissue is required to elicit the desired biological response. Imaging of bone metastases and treatment of bone resorption disorders with La^{3+} are applications that illustrate this point. In these cases, chelators chauffeur (radio)metal ions to regions with an abnormally high bone growth rate or rapid bone turnover. Upon release, the (radio)metal ions may become adsorbed onto bone or even incorporated into hydroxyapatite (HA, the mineral matrix that makes up cortical bone), where they can evoke a localized response.[4] Moreover, chelators may be used to decrease unusually high levels of free metal ions in vivo, as is commonly achieved during chelation therapy. In this case, toxic
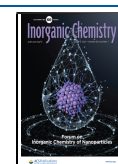
Chart 1. Examples of Multidentate Ligands and Their Potential Medical Applications[a]

Targeted Radiopharmaceuticals

Ligand: H$_4$octapa

☢ = ^{111}In, ^{177}Lu, ^{90}Y, ^{225}Ac

R = peptide, antibody, etc.

Magnetic Resonance Imaging

Ligand: DTPA

Chelation Therapy

Ligand: DMSA

M = Hg^{2+}, Pb^{2+}

Palliative Bone Therapy

Ligand: EDTMP

☢ = ^{153}Sm, ^{177}Lu

Bone Resorption Therapy*

Ligand: XT
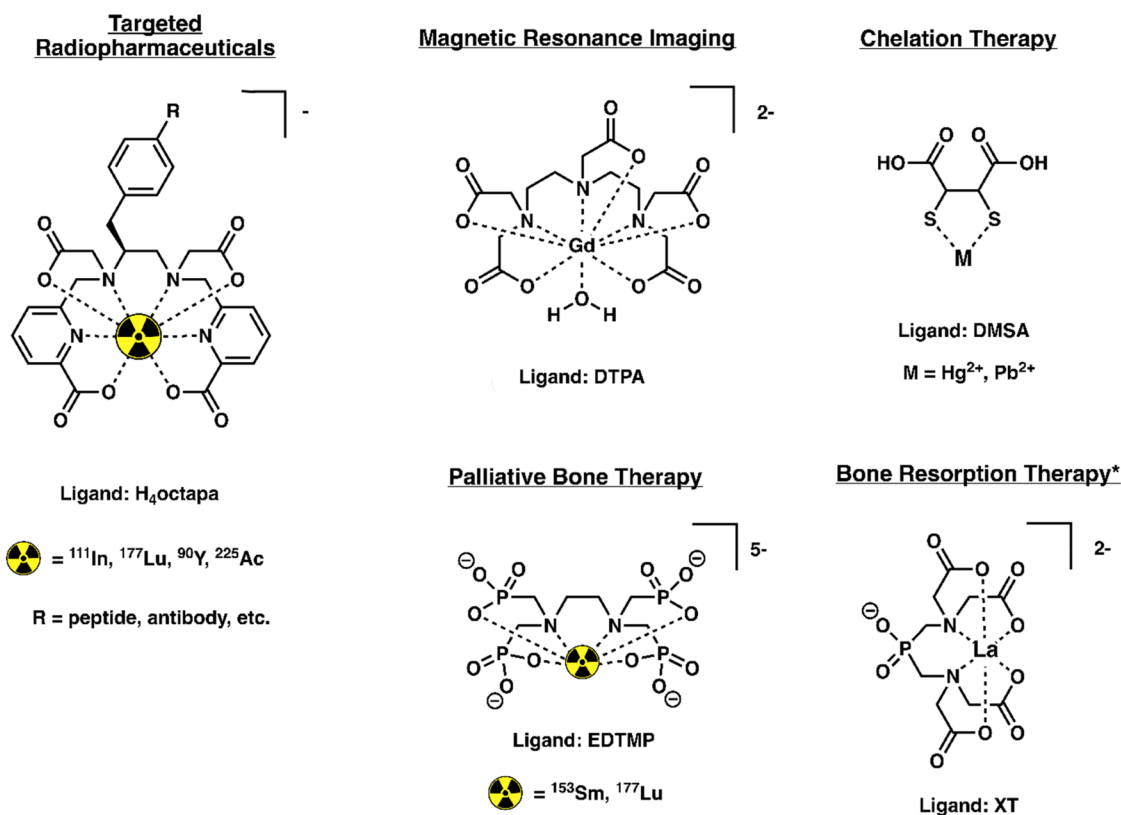
[a](*) Under investigation; not clinically tested.[7]

concentrations of endogenous (e.g., Fe^{3+}, Cu^{2+}) or exogenous (e.g., Pb^{2+}, Hg^{2+}) metal ions can be diminished through an administration of chelators to sequester free metal ions and more rapidly excrete them, mitigating deleterious effects such as an excessive formation of reactive oxygen species (ROS).[5,6] Chelators also serve in many useful roles outside the medical realm (e.g., water treatment, heavy metal extraction); however, for brevity, these topics will not be discussed further here. Clearly, chelators offer much utility to the medical world and beyond (Chart 1).

Phosphonate-bearing chelators have seen continued interest over recent years due to their well-known "hard" (predominantly ionic) coordination electronics as well as their rapid kinetics of complexation.[8,9] In comparison to more commonly employed carboxylic acids, phosphonates are particularly well-suited toward the coordination of hard metal ions, such as small high-valent main-group (e.g., Ga^{3+}, Al^{3+}) and transition metals (e.g., Fe^{3+}, Sc^{3+}) as well as the entire lanthanide series.[10] Another interesting feature of (bis)phosphonates is their natural tendency to interact with bone. Phosphonates are a fundamental component of HA (along with Ca^{2+} and OH$^-$), and so naturally their interactions have been studied to investigate any medicinal properties that can be harnessed to treat bone disorders.[4] While the long-term efficacy remains unclear,[11] bisphosphonates such as alendronate (trade name: Fosamax) have long been established as agents capable of increasing the bone density in patients suffering from osteoporosis.[12,13] Taken together, the hard and labile coordination properties of phosphonates, along with their affinity toward HA, has led to their elegant application as metal-based bone-targeting agents. [^{153}Sm][Sm(EDTMP)]$^{5-}$

and (more recently) [^{177}Lu][Lu(EDTMP)]$^{5-}$ are prime examples of multifunctional phosphonate species.[14,15] Not only does (P–O)$_x$ → M^{3+} (M = Sm, Lu) coordination form the majority of the energetic drive for this species to exist but the delivery of the radionuclides to their target (i.e., bone metastases) is also firmly rooted in phosphonate-dominated interactions. It is worth noting that noncoordinating (bis)-phosphonate donors are better-suited for bone targeting, while metal coordination can mitigate this targeting effect and instead permit bioconjugate-dominated bioactivity.[16–18] Another method to stifle bone targeting is the use of phosphinate groups, which present a convenient handle for bifunctionalization if targeted radionuclide delivery is the goal. Phosphonate P–OH bonds are commonly converted to P–CH$_2$–R bonds, where R leads to a group capable of covalent linkage (e.g., NCS, COOH, maleimide, alkyne) with a targeting vector.[19–23] This conversion is generally synthetically straightforward and helps shorten the time between the identification of a promising chelator and in vivo trials. Clearly, phosphonates are multifaceted functional groups whose application in chelating ligands warrants further investigation.

Picolinic acids are another motif commonly found in modern chelators. Their broad applicability[24–30] has led to a tremendous number of chelator variants; however, a very few bearing both picolinic and phosphonic acids have been reported. H$_6$phospa is a well-known derivative due to its simplicity of design, and it was originally studied as a Gd^{3+}-based contrast agent.[31] As a BFC for radiopharmaceuticals, incompatibility with [^{89}Zr]Zr^{4+} and complex lability with [^{111}In]In^{3+} and [^{177}Lu]Lu^{3+} when conjugated to trastuzumab (HER2/*neu*-targeting monoclonal antibody; mAb) have been

**Chart 2. Phosphonate-Bearing Picolinic Acid-Derived Chelators[a]**
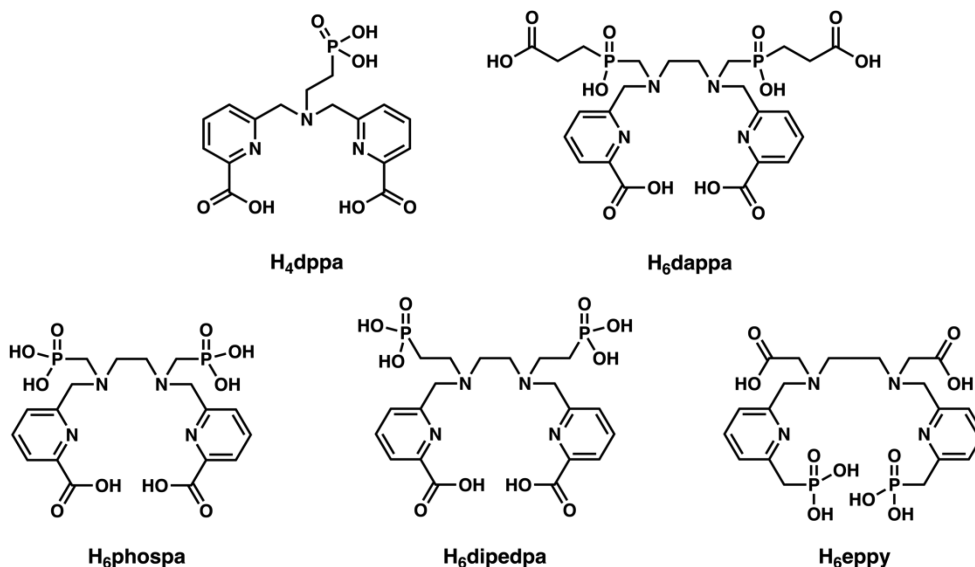
[a](top) Previously reported (not described). (bottom) Under investigation in this work.

reported.[32] No investigation of H$_6$phospa thermodynamic parameters have been explored. Another more recent report is of the phosphinate-bearing picolinic acid derivative H$_6$dappa.[33] While a similar lability with [^{111}In]In^{3+} was reported, in-depth thermodynamic studies and density functional theory (DFT) calculations provide insight into the reason behind the complex's low kinetic inertness and how to mitigate lability if desired. Lastly, H$_4$dppa is a condensed, hexadentate scaffold intended for use with [^{68}Ga]Ga^{3+} as well as for the potential delivery of La^{3+} to HA for the treatment of bone resorption disorders.[34]

Herein, we report the synthesis and characterization of three ligands, namely, H$_6$phospa, H$_6$dipedpa, and H$_6$eppy (Chart 2), in order to study the effect that structural differences have on the coordination chemistry and future ligand application. Crystal structures of the first two ligands were obtained. The metal complexation of these three molecules was investigated by NMR spectroscopy with five trivalent metal ions of varying sizes and electronics (i.e., In^{3+}, Lu^{3+}, Y^{3+}, Sc^{3+}, and La^{3+}). Thermodynamic parameters (log K_{ML} and pM) were calculated for all 15 complexes and were used to compare and rationalize the stability across varying ligand and metal series. DFT structures of several La^{3+} and Sc^{3+} complexes were calculated, and some were validated through a comparison of experimental and theoretical NMR spectra. Lastly, binding energies of several complexes were calculated from DFT structures.

RESULTS AND DISCUSSION

Ligand Synthesis and Characterization. The strategy for the synthesis of H$_6$phospa and H$_6$dipedpa (Scheme 1) was to build first the dipicolinate ethylenediamine scaffold through the synthesis of **1** (as reported elsewhere[32,33]) and then to functionalize the resultant secondary amines to yield two distinct ligands, differing only in the length of the amine-phosphonate bridging unit. H$_6$phospa was synthesized via a Kabachnik-Fields reaction, which forms a methylene bridge between the amine and phosphonate group following the dissolution and heating of **1** and phosphorous acid in

Scheme 1. H$_6$phospa and H$_6$dipedpa Syntheses
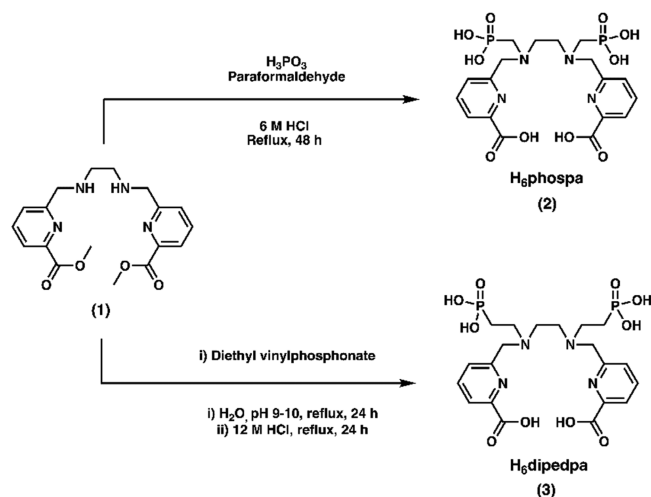
hydrochloric acid (HCl; 6 M) and the slow addition of paraformaldehyde. The harsh conditions required for this reaction also conveniently deprotect the methyl esters of **1**, obviating a step. H$_6$dipedpa was synthesized through an aza-Michael addition between **1** and diethyl vinylphosphonate in a refluxing aqueous solution at pH 9−10 to ensure an adequate nucleophilicity of secondary amines. Upon addition of two phosphonate arms, the excess diethyl vinylphosphonate can be extracted with dichloromethane. Although the intermediate is somewhat hydrophobic due to the pyridine rings and ethyl-protected phosphonate groups, the picolinic acid groups become deprotected under reaction conditions due to the combination of basic pH and high heat, as supported by mass spectroscopy (low-resolution electrospray ionization mass spectrometry (LR-ESI-MS)). This results in the desired intermediate remaining in the aqueous phase. Deprotection of the phosphonate groups is achieved through the rotary evaporation of solution followed by the addition and refluxing of concentrated (conc) HCl. Unlike most other picolinic acid ("pa") family ligands, H$_6$phospa and H$_6$dipedpa do not require

Scheme 2. H$_6$eppy Synthesis
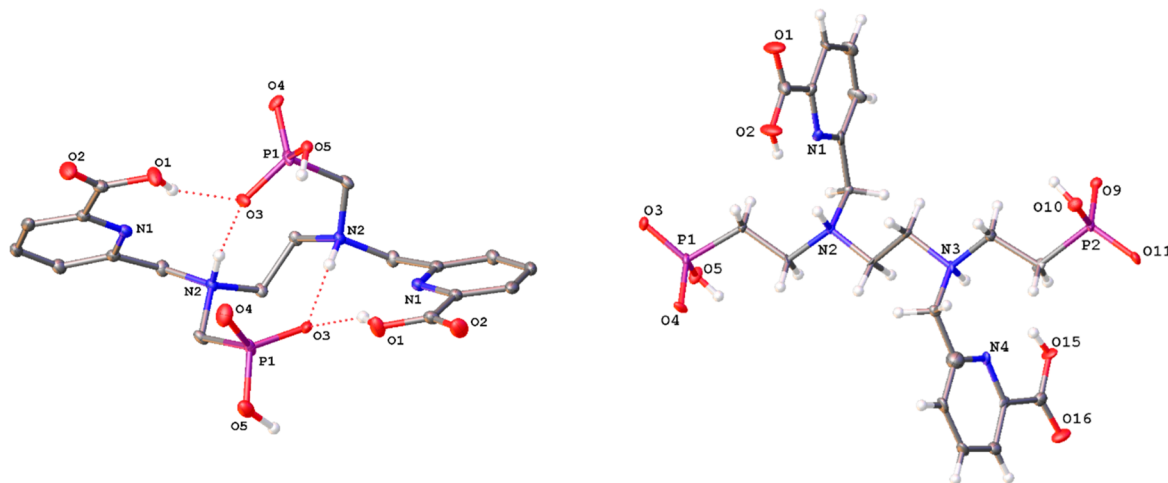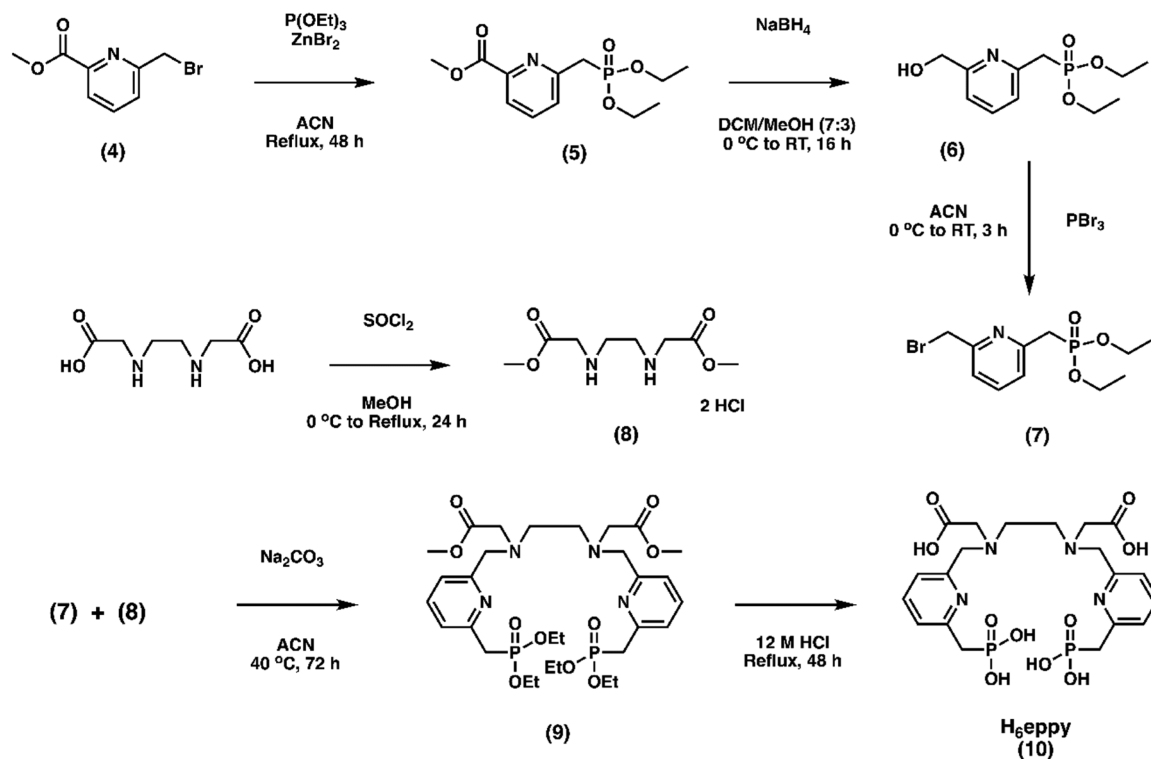
Figure 1. ORTEP diagrams of H$_6$phospa (left) and H$_6$dipedpa (right).

high-performance liquid chromatography (HPLC) for purification; the phosphonate groups on both ligands instead enable the use of a two-solvent precipitation to yield pure products. Following the HCl reflux and the complete evaporation of solvent, dissolving the crude product in minimal water, then precipitating out the product with acetone yields a crude brown oil once the precipitate is allowed to settle. Decanting of the solution and washing the oil with acetone yields the pure ligand as a hydrated HCl salt (i.e., H$_6$phospa·0.3HCl·1.8H$_2$O and H$_6$dipedpa·4HCl·2H$_2$O). The simplicity of these syntheses and the luxury of obviating time-consuming HPLC purification are very attractive features indeed.

H$_6$eppy is a unique derivative in the pa family of ligands, as the picolinic acid groups have been replaced with pyridine-methylenephosphonates. While (by definition) it is not part of

the pa family, H$_6$eppy does provide an interesting comparative study with the aforementioned ligands and was therefore the aim of this synthetic endeavor. Similar to the synthesis of H$_6$phospa and H$_6$dipedpa, the strategy to make H$_6$eppy (Scheme 2) was to base the design around an ethylene diamine backbone and add the desired arms sequentially. Taking inspiration from the optimized synthesis of H$_4$octapa,[35] instead of adding acetate arms to a protected ethylene diamine starting material, a simple Fischer esterification of ethylenediamine-N,N′-diacetic acid (EDDA) resulted in the desired backbone (**8**), with secondary amines available for subsequent arm attachment via S$_N$2. The synthesis of the pyridine-phosphonate arm (**7**) builds upon the methyl-6-bromomethylpicolinate arm (**4**) used in the above syntheses. With triethylphosphite and zinc(II) bromide as a catalyst, the Michaelis-Arbuzov reaction
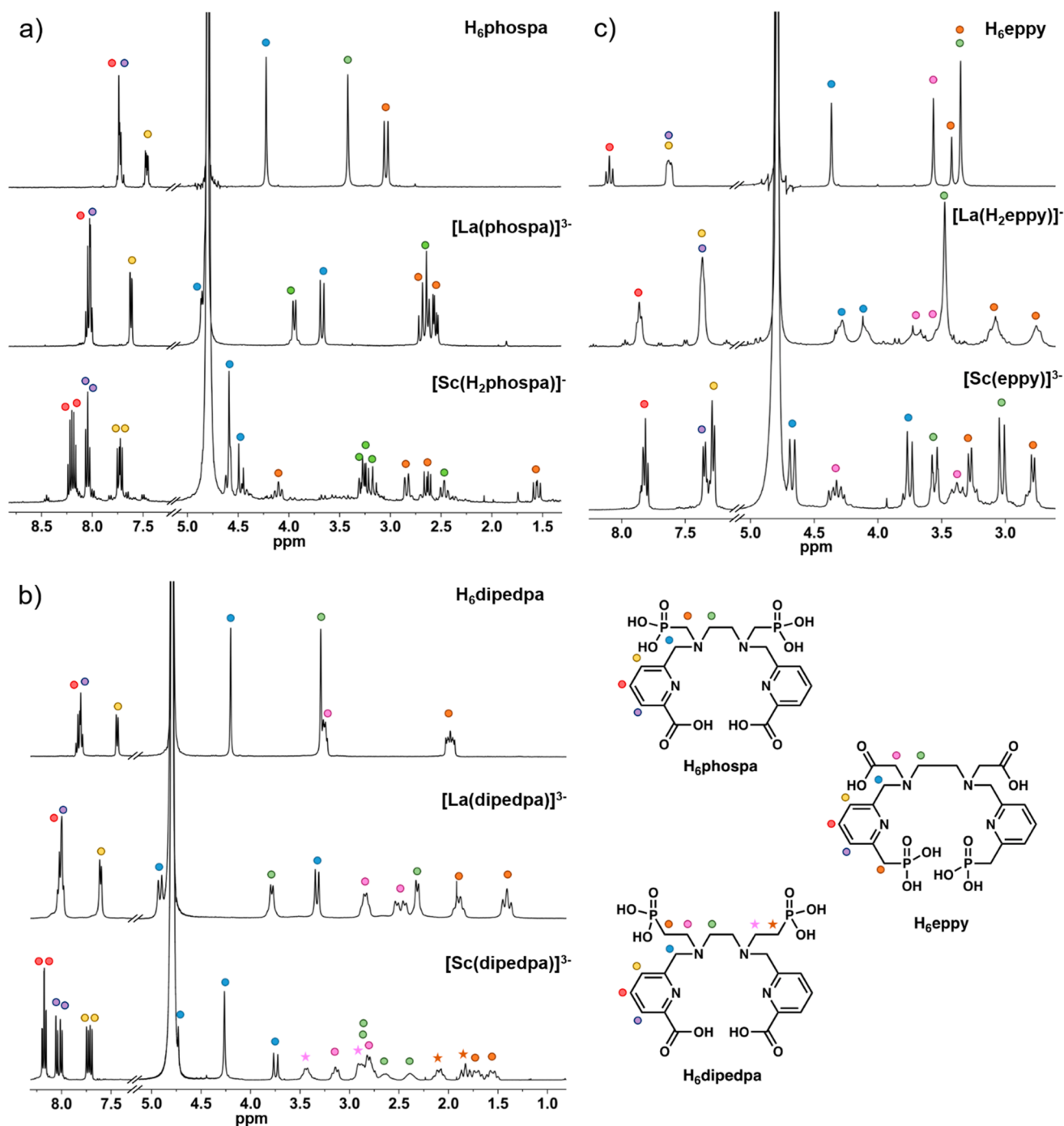
Figure 2. ^{1}H NMR spectra of (a) H$_6$phospa, (b) H$_6$dipedpa, and (c) H$_6$eppy and their corresponding La^{3+} and Sc^{3+} complexes (D$_2$O, 25 °C, 400 MHz); stars in the [Sc(dipedpa)]$^{3-}$ spectrum represent neighboring ethylene protons of the asymmetric complex. Labels indicate dominant metal complexes in solution. See Figures S47–S61 for complete speciation diagrams.

results in a replacement of the bromine group with a protected phosphonate. The reduction of the methyl ester with NaBH$_4$ primes the alcohol for a bromination with PBr$_3$. Note that **7** is prone to decomposition, as reported by Abada et al.[36] Thus, immediately following its synthesis, the arm was combined with **8** to produce the protected ligand (**9**). For this reaction, the temperature is crucial, as temperatures above 40 °C were noted to complicate the ensuing purification. It is speculated that a high temperature promotes the cyclization of backbone **8**, which is then exceedingly difficult to separate from the desired product. Lastly, deprotection is achieved by dissolving

9 in conc HCl and then refluxing for 48 h. Similar to the purification of H$_6$phospa and H$_6$dipedpa, crude H$_6$eppy can be purified by a dissolution in minimal water and precipitated with acetone. After the accumulation of precipitate as droplets of brown oil, the solution can be decanted, yielding the pure ligand as an HCl salt (H$_6$eppy·4.5HCl·3H$_2$O) following additional washing with acetone and lyophilization.

X-ray Crystal Structures. X-ray quality single crystals of both H$_6$phospa and H$_6$dipedpa were obtained through the two-vial vapor diffusion technique, where acetone slowly diffused into an aqueous solution containing the compound of
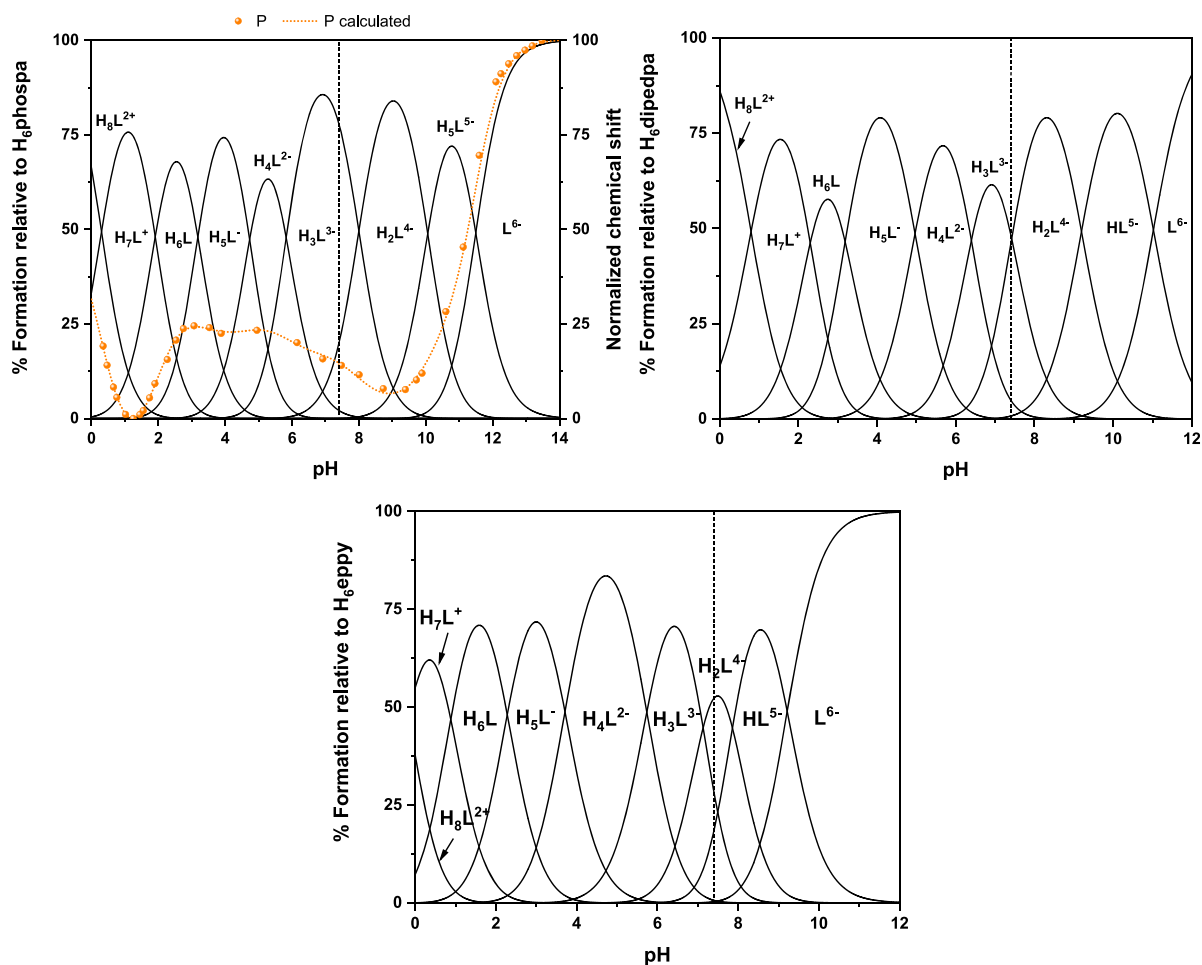
Figure 3. Speciation plots of H_6phospa, H_6dipedpa, and H_6eppy. [31]P chemical shift dependence on the pH of H_6phospa and HypNMR2008[43] fitting overlaps the speciation plot; the dashed line indicates the physiological pH of 7.4.

interest, with an approximate concentration of 8 mM and no further adjustment of pH. The Oak Ridge Thermal-Ellipsoid Plot (ORTEP) diagrams of the ligands are shown in Figure 1. Crystallographic information and selected bond lengths/angles can be found in Tables S2−S6. From Figure 1, it can be seen that H_6phospa and H_6dipedpa are neutral, zwitterionic species (deprotonated phosphonates; protonated amines) consistent with calculated pK_a values (vide infra), given the pH ≈ 2 solution from which the crystals were grown. The configuration of H_6phospa reveals a symmetric, closed-structure conformation with an intramolecular hydrogen bonding between the protonated picolinic acid, deprotonated phosphonate, and protonated amine groups. Conversely, the configuration of H_6dipedpa is a symmetric, open-chain structure, with evident phosphonate-water hydrogen-bonding (shown in Figure S62) in lieu of intramolecular interactions.

Metal Complexation Studies. Complexation studies were conducted primarily through the use of ^{1}H NMR spectroscopy and [1]H−[1]H correlation spectroscopy (COSY) as well as ^{31}P{^{1}H} NMR spectroscopy and high-resolution electrospray ionization mass spectrometry (HR-ESI-MS). These studies were performed not only to confirm the metal chelation but also to gain insight into the complex symmetry, fluxionality, and approximate ligand configurations in solution. The trivalent metal ions In^{3+}, Sc^{3+}, Lu^{3+}, and Y^{3+} were selected because of the availability of radioisotope counterparts (i.e.,

$[^{111}In]In^{3+}$, $[^{44}Sc]Sc^{3+}$, $[^{177}Lu]Lu^{3+}$, and $[^{90}Y]Y^{3+}$), which have varying degrees of clinical utility, ranging from primarily preclinical research (e.g., $[^{44}Sc]Sc^{3+}$) to routine clinical use (e.g., $[^{177}Lu]Lu^{3+}$). Moreover, La^{3+} was studied (in the absence of a more suitable candidate) as it is considered a "cold" surrogate for the now-famous α-emitter, $[^{225}Ac]Ac^{3+}$. Additionally, excluding In^{3+}, this series of (pseudo)lanthanides presents an opportunity to study how an ionic radius impacts the chelation chemistry, as size increases across the series, yet chemical hardness remains virtually identical (as measured by the Drago−Wayland metric I_A).[10]

Typical evidence of ligand chelation is a qualitative observation of diastereotopic splitting in ^{1}H NMR spectra, which can be confirmed by [1]H−^{1}H COSY. These splitting patterns are a result of previously equivalent protons of freely rotating and symmetric ligands (often C_{2v} point groups for pa ligands) becoming inequivalent due to metal ion chelation, which results in structural rigidity. For example, the observation of a singlet peak in the ^{1}H NMR spectra of a free ligand being replaced by two doublet peaks (each with a half integration of the singlet) following the addition of metal ion is a common sign of chelation. For symmetric complexes, the simplicity of resulting splitting patterns often makes spectra straightforward to interpret. When metal complexes are asymmetric, however, the interpretation can be more

Table 1. Protonation Constants (log K_a) of the Discussed Ligands

equilibrium reaction	H₆phospa	H₆dipedpa	H₆eppy
$L^{6-} + H^+ \leftrightarrows HL^{5-}$	11.43 (1)[a]; 11.50 (1)[b](N_en)	11.02 (1)[b](N_en)	9.22 (1)[b](N_en)
$HL^{5-} + H^+ \leftrightarrows H_2L^{4-}$	10.05 (1)[b](N_en)	9.20 (1)[b](N_en)	7.86 (1)[b](P–OH)
$H_2L^{4-} + H^+ \leftrightarrows H_3L^{3-}$	8.00 (2)[b](P–OH)	7.42 (1)[b](P–OH)	7.13 (1)[b](P–OH)
$H_3L^{3-} + H^+ \leftrightarrows H_4L^{2-}$	5.83 (2)[b](P–OH)	6.40 (1)[b](P–OH)	5.74 (1)[b](N_en)
$H_4L^{2-} + H^+ \leftrightarrows H_5L^{-}$	4.73 (1)[b](py-COOH)	4.97 (1)[b](py-COOH)	3.71 (1)[b](COOH)
$H_5L^{-} + H^+ \leftrightarrows H_6L$	3.18 (2)[b](py-COOH)	3.19 (1)[b](py-COOH)	2.29 (2)[b](COOH)
$H_6L + H^+ \leftrightarrows H_7L^{+}$	1.85 (9)[b](P–OH)	2.30 (2)[b](P–OH)	0.88 (3)[c](P–OH)
$H_7L^{+} + H^+ \leftrightarrows H_8L^{2+}$	0.3 (1)[a](P–OH)	0.8 (1)[c](P–OH)	−0.16 (2[c](P–OH)
$\sum \log K \; \{[H_iL]/[H_{q-1}L][H^+]\}$	45.37 (1);45.44 (1)	45.3 (1)	36.67 (2)

[a]Using ^1H and ^{31}P NMR titrations. [b]Using UV-potentiometric titrations. [c]Using UV batch titration, T = 25 °C, I = 0.16 M NaCl (when possible).

challenging due to the twofold increase in signals, which can overlap and become difficult to differentiate.

Figure 2 illustrates characteristic spectral changes as a result of chelation, both from symmetric and asymmetric complexes. Lanthanum(III) complexes derived from pa family chelators are often rigid and symmetric as a result of the lanthanum large radius (1.16 Å, coordination number (CN) = 8),[37] which fills the dedpa-like (N,N'-dipicolinate ethylenediamine)[25] coordination sphere and permits facile coordination of pendant arms to (near) coordinatively saturate the metal ion. Indeed, both H₆phospa and H₆dipedpa conform to this tendency, as supported by simple diastereotopic splitting patterns in ^1H NMR spectra. Medium-sized metal ions (e.g., Y^{3+}, In^{3+}, Lu^{3+}) have less predictable behavior with the pa family of chelators, as small differences in functional groups have historically led to a range of behaviors with respect to isomers, fluxionality, and symmetry,[38−41] as is the case with the pa ligands studied in this work (see Figures S19−S42 for NMR spectra of these complexes). Scandium(III) complexes of pa family ligands have only recently[42] seen interest due to the increasing availability of $[^{44/47}Sc]Sc^{3+}$. Interestingly, with both H₆phospa and H₆dipedpa, resulting Sc^{3+} complexes are rigid and asymmetric. Figure 2a,b illustrates the differences in spectral complexity between these symmetric La^{3+} and asymmetric Sc^{3+} complexes.

While the coordinating functional groups of H₆eppy are identical to those of H₆phospa and H₆dipedpa [$N_4O_2(PO)_2$], the rearrangement of phosphonate and carboxylate groups excludes H₆eppy from the pa family and has led to a number of interesting differences in metal ion chelation. The most striking difference comes from a comparison of the Sc^{3+} complexes. Scandium(III) complexes of H₆phospa and H₆dipedpa are asymmetric, likely as a result of the pyridine rings conforming to a perpendicular coordination environment (~90° N_{py}–Sc–N_{py} bond angle) to accommodate the small metal ion (Sc^{3+} ionic radius = 0.87 Å, CN = 8),[37] which does not adequately fill the usual dedpa-like coordination sphere. Conversely, replacement of the aromatic carboxylic acids with methylene-bridged phosphonate groups results in less contortion of the pyridine rings and ethylene backbone as a result of the additional points of free rotation (i.e., py-**CH₂**-P(O)(OH)₂). As supported by the simple diastereotopic splitting seen in Figure 2c, a rigid, symmetric Sc^{3+} complex is the result of this alteration. The relative broadness of the $[La(H_2eppy)]^-$ complex can also be rationalized when considering the ligand

flexibility. The rigid nature of picolinic acid groups and the close match of La^{3+} to the binding pocket of pa family ligands generally lead to symmetric and highly rigid La^{3+} complexes, as seen in Figure 2a,b. While H₆eppy appears to maintain the symmetry when chelating La^{3+}, the peak broadness in the ^1H NMR spectrum suggests a fluxional behavior of the complex, which is logically a result of a decreased ligand rigidness.

Solution Thermodynamics of H₆phospa, H₆dipedpa, and H₆eppy. Since the basicity of different donor atoms of the ligand affects metal complexation, detailed protonation constants of H₆phospa, H₆dipedpa, and H₆eppy were determined. For each of the ligands, 10 protonation sites are possible; however, even in very acidic solutions, protonation constants of the two most acidic donor atoms were not accessible. Thus, at that acidic pH, those donor atoms are deprotonated and can readily coordinate metal ions. For each ligand, two different methods were used for the pK_a determination: acidic UV-in-batch spectrophotometric titrations and combined UV-potentiometric titrations. The spectral evolution of each ligand, with respect to pH, and the corresponding speciation plots are shown in Figures S44− S46. For H₆phospa, additional ^{31}P and ^1H NMR titrations were performed to assign more accurately and determine the most acidic and most basic pK_a values (Figures 3 and S43).

Because of the structural similarity of the three ligands, comparisons can be made to investigate the influence of the substituent position and nature on ligand protonation constants and the metal coordination. H₆phospa and H₆dipedpa differ in the amine−phosphonate bridging group. H₆phospa has a methylene bridge, while H₆dipedpa has an ethylene bridge (Chart 2). The most basic groups in these ligands are the tertiary N atoms (N_{en}) in the ethylenediamine backbone. The basicity of those amines in H₆phospa (log K_1 = 11.43(1); 11.50(1); log K_2 = 10.05(1)) are greater than those in H₆dipedpa (log K_1 = 11.02(1); log K_2 = 9.20(1)). This is due to the greater stabilization offered by the strong intramolecular hydrogen-bond interactions of the phosphonates in H₆phospa with the protonated tertiary amines. This explanation is supported by the X-ray structure of the ligand (Figure 1). $^{31}P\{^1H\}$ NMR and ^1H NMR titrations of H₆phospa support the existence of H-bond interactions in these protonation steps, as a large change in the ^{31}P chemical shift occurs in the range of 10 < pH < 12 (Figures 3 and S43). Protonation constants of the phosphonate functionalities for H₆phospa and H₆dipedpa are close to those found for similar

Table 2. Stability Constants (log K_{ML}) and the Corresponding Stepwise Protonation Constants log $K_{1q1}(MH_qL)^a$ of H$_6$phospa, H$_6$dipedpa, and H$_6$eppy with Metal Ions of Interest^b

	Sc^{3+}	In^{3+}	Lu^{3+}	Y^{3+}	La^{3+}
			H$_6$phospa		
log K_{101}(ML)	**34.92 (3)**	**38.64 (3)**	**29.90 (6)**	**28.01 (4)**	**27.99 (4)**
log K_{111}(MHL)	5.94 (4)	5.45 (6)	6.47 (7)	6.19 (1)	5.41 (1)
log K_{121}(MH$_2$L)	4.28 (4)	4.06 (3)	4.07 (6)	4.68 (2)	4.57 (3)
log K_{131}(MH$_3$L)	2.96 (2)	2.98 (3)	3.55 (1)	2.38 (2)	2.97 (2)
log K_{1-11}(M(OH)L)	9.65 (4)	10.43 (3)	9.48 (7)	11.44 (4)	10.54 (4)
			H$_6$dipedpa		
log K_{101}(ML)	**25.17 (3)**	**31.12 (2)**	**23.96 (3)**	**23.90 (2)**	**25.82 (3)**
log K_{111}(MHL)	6.59 (3)	6.93 (2)	7.13 (3)	7.11 (2)	4.71 (2)
log K_{121}(MH$_2$L)	4.52 (2)	4.11 (2)	5.00 (1)	4.74 (2)	3.40 (3)
log K_{131}(MH$_3$L)	3.05 (2)	3.19 (1)	2.76 (1)	2.89 (3)	3.40 (3)
log K_{1-11}(M(OH)L)	8.08 (2)	8.74 (3)	9.17 (3)	9.47 (3)	7.02 (3)
log K_{1-21}(M(OH)$_2$L)	9.76 (2)				10.22 (3)
			H$_6$eppy		
log K_{101}(ML)	**22.03 (2)**	**26.56 (2)**	**18.44 (3)**	**17.85 (1)**	**15.60 (2)**
log K_{111}(MHL)	4.74 (4)	6.40 (2)	8.29 (3)	8.45 (1)	7.32 (2)
log K_{121}(MH$_2$L)	4.35 (3)	4.35 (3)	4.42 (4)	4.01 (1)	5.26 (2)
log K_{131}(MH$_3$L)	3.06 (4)	2.88 (3)			
log K_{1-11}(M(OH)L)	7.73 (2)	8.62 (3)	10.65 (5)	10.65 (2)	10.73 (2)
log K_{1-21}(M(OH)$_2$L)	9.93 (3)				

$^a K_{1q1} = [MH_qL]/[MH_{q-1}L][H]^q$; $(q - 1) = -1$ denotes OH. $^b T = 25$ °C, $I = 0.16$ M NaCl.

ligands (Table 1).[9,34] The differences in phosphonate protonation constants between H$_6$phospa (log K_3 − log K_4 = 2.17) and H$_6$dipedpa (log K_3 − log K_4 = 1.02) are worth noting and are explained by the higher intramolecular hydrogen-bond interaction in H$_6$phospa, together with the higher charge repulsion with the closer phosphonate moieties. Following those protonations are the pyridylcarboxylic acid substituents (py-COOH), which compared to the ones in H$_4$octapa[35,38] are slightly higher. Finally, the protonation constants for the most acidic phosphonates in both ligands are comparable, with the H$_6$phospa values being slightly more acidic. The protonation scheme of H$_6$phospa, assignments, and values are confirmed through the dependence of experimental chemical shifts on pH in ^{31}P NMR and ^{1}H NMR titrations.

Another effect on pK_a caused by the replacement of substituents can be observed by comparing H$_6$phospa with H$_6$eppy. The exchange of the carboxylic acid in the pyridine ring for a phosphonic acid drastically lowers the overall ligand basicity (Table 1). The higher protonation constants found for the N$_{en}$ atoms in H$_6$phospa now are reduced ∼2.28 units for the most basic proton (log K_1 = 9.22) and 4.31 units for the second most basic proton (log K_4 = 5.74). This is reasonable and supported by the H-bond interaction between the N$_{en}$ and the phosphonate groups in H$_6$phospa, which are presumably absent in H$_6$eppy. These lower pK_a values of H$_6$eppy are very close to those of H$_4$octapa[35] due to their identical ethylenediamine diacetic acid backbone. In H$_6$eppy, protonation constants of the phosphonate substituents (log K_2 = 7.86; log K_3 = 7.13) are closer to one another than in H$_6$phospa, and they are followed by the protonation of the carboxylic acid substituents (log K_5 = 3.71; log K_6 = 2.29). The most acidic protons are most likely bound to the remaining phosphonate groups (log K_7 = 0.88; log K_8 = −0.16).

We recently reported the decadentate phosphinate-containing ligand H$_6$dappa[33] (Chart 2), which can also be compared with H$_6$phospa. The substitution of a carboxyethyl phosphinic acid for a phosphonic acid in H$_6$phospa greatly increases the

basicity of the N$_{en}$ atoms (from log K_1 = 7.96(1) and log K_2 = 5.48(2) to log K_1 = 11.43(1) and log K_2 = 10.05(1)) and the overall basicity over those two steps log β_2 (from 13.44(1) to 21.48(1)) due to the electronic differences between phosphonates and phosphinates, as well as the hydrogen bonding present in H$_6$phospa.

A final comparison between H$_6$dipedpa and its smaller analogue H$_4$dppa[34] can be made. The ethylenediamino-N,N'-diethyl phosphonic acid backbone, as opposed to the aminoethyl phosphonic acid, not only increases the overall basicity but also the coordination number and the metal complex stability with lanthanum ions. Nonetheless, H$_6$dipedpa and H$_4$dppa share the same protonation scheme, with the most acidic pK_a belonging to the phosphonate group(s), followed by both picolinic acid protonation constants, then the more basic phosphonates. Lastly, in each case the amine backbone has the most basic pK_a value(s) of each ligand. Because of the very acidic phosphonate protons, H$_4$dppa protonation constants were obtained using both potentiometric and ^{31}P/^{1}H NMR titrations.[34]

■ COMPLEX FORMATION EQUILIBRIA OF H$_6$PHOSPA, H$_6$DIPEDPA, AND H$_6$EPPY WITH IN^{3+}, LU^{3+}, Y^{3+}, SC^{3+}, AND LA^{3+}

Complex formation equilibria of H$_6$phospa, H$_6$dipedpa, and H$_6$eppy with Sc^{3+}, In^{3+}, Lu^{3+}, Y^{3+}, and La^{3+} were studied through combined UV-potentiometric titrations, and for metal complexes where complexation occurred below the electrode threshold, acidic UV-in-batch spectrophotometric titrations were performed to determine the first protonated metal complex species. Stability constants were calculated with HypSpec2014[44] and Hyperquad2013[45] (Table 2), and the speciation plots were generated with Hyss.[46] For all three ligands, metal complexes species [M(H$_3$L)], [M(H$_2$L)]$^−$, [M(HL)]$^{2−}$, [ML]$^{3−}$, and [M(OH)L]$^{4−}$ were identified, as well as [M(OH)$_2$L]$^{5−}$ for H$_6$dipedpa and H$_6$eppy.
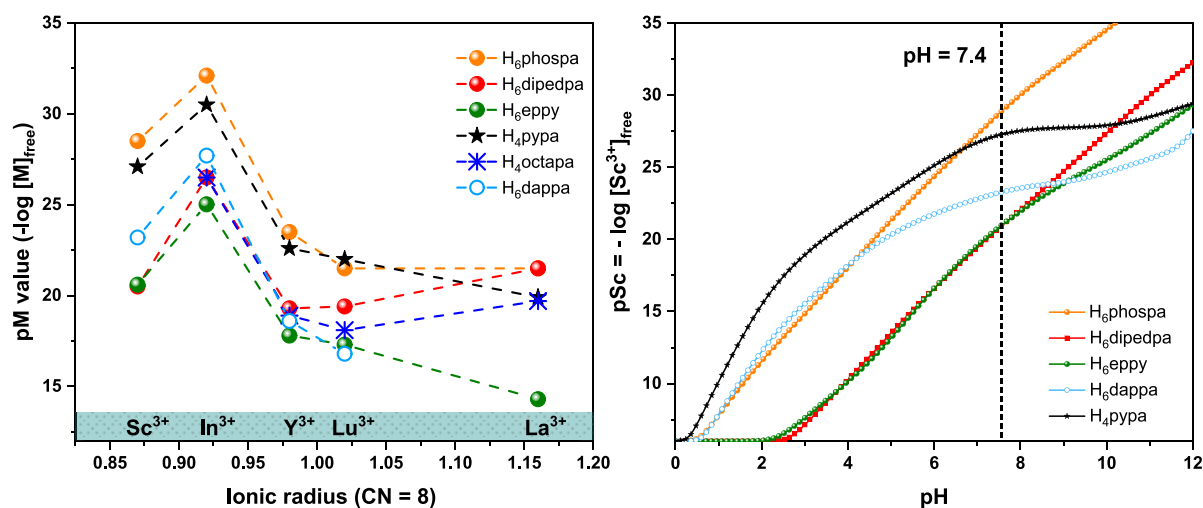
Figure 4. pM values (M^{3+} = Sc^{3+}, In^{3+}, Y^{3+}, Lu^{3+}, La^{3+}) vs ionic radii (CN = 8) for discussed chelating ligands (left) and the Sc^{3+} scavenging ability of the discussed ligands with pH (right). Dashed line indicates the physiological pH of 7.4.

Metal complex stability for the three ligands follows the order H_6phospa > H_6dipedpa > H_6eppy. It is worth noting that, despite the equal overall basicity of H_6phospa and H_6dipedpa, complex formation equilibria are energetically more favored for H_6phospa. Complex formation of H_6phospa for each of the metal ions starts at a lower pH than the corresponding ones for H_6dipedpa or H_6eppy. Additionally, from Table 2 it can be noted that, when comparing H_6phospa and H_6dipedpa metal complexes, protonation constants of $[M(HL)]^{2-}$ and $[M(H_2L)]^-$ species are comparable for both ligands. The major difference lies in the protonation of the $[ML]^{3-}$ species for each of the metal ions (excluding La^{3+}), which is higher for H_6dipedpa, ultimately leading to a higher stability of the $[ML]^{3-}$ species for H_6phospa complexes.

When comparing the metal complex stability with different chelating ligands, a superior metric to log K_{ML} is the pM value. Not only is pM linearly correlated to the stability of metal complexes but it also accounts for the ligand basicity, denticity, and stoichiometries of metal complexes. pM is defined as $-\log[M]_{free}$ at (mostly) standard conditions ($[L] = 10$ μM, $[M] = 1$ μM and pH = 7.4).[47] It is generally considered as the metal scavenging ability of a ligand (the lower the $[M]_{free}$, the higher the pM) and allows the comparison of both the affinity of different ligands for a specific metal ion as well as the metal selectivity of a ligand for different metal ions. Figure 4 is a plot of pM values (M = Sc^{3+}, In^{3+}, Lu^{3+}, Y^{3+}, La^{3+}) for the ligands studied in this work, as well as similar ligands developed for use as radiopharmaceutical agents. For H_6phospa, H_6dipedpa, and H_6eppy, pM follows the trend pIn > pSc > pLu > pY > pLa, with the exception of H_6dipedpa, for which pLa is higher than pY and pLu. More interesting however is Figure 4, where the free metal (pSc) has been plotted versus pH for comparable chelators. In addition to comparing the metal scavenging ability of different chelators at pH 7.4 (essential in medicinal applications to avoid transmetalation reactions in vivo), the pM value allows for the quantification of the free metal ions from pH 0 to 12. This can be useful when a high selectivity is required at a specific pH (e.g., radionuclide purification, water purification, biological media). It is interesting to note the different profiles of the curves. For ligands like H_6dappa and H_4pypa with similar and lower overall basicities (Table S1), pSc grows from lower pH exponentially, reaching a plateau

before pH 7.4, while for more basic ligands like H_6phospa, H_6dipedpa, and H_6eppy, pSc follows a continued exponential growth. This reflects how ligands with lower overall basicities have less proton competition for the metal ion and have a broader pH range with a static complex stability (due to the stability plateau). On an encouraging note, as shown by the graph, H_6phospa has the highest pSc value reported at physiological pH and above, which provides auspicious evidence for further study with the theranostic radionuclide pair $[^{44/47}Sc]Sc^{3+}$.

Density Functional Theory Calculations. The structures, coordination geometries, free energies, and theoretical NMR spectra of $[La(H_q\text{phospa})(H_2O)]^{(q-3)}$, $[Sc(H_q\text{phospa})]^{(q-3)}$, $[La(H_q\text{dipedpa})]^{(q-3)}$, and $[Sc(H_q\text{dipedpa})]^{(q-3)}$ were studied using DFT calculations at the PBE0-D3/def2-TZVP level of theory in a range of protonation states (large basis sets with effective core potentials were used for the metal ions; see the Experimental Section for details). These complexes were chosen because of the interesting features noted in their ^{1}H NMR spectra. Moreover, as rare-earth ions, La^{3+} and Sc^{3+} have a similar ionic bonding character despite their drastic differences in ionic radii.[10,37] Thus, a comparison of La^{3+} and Sc^{3+} metal complexes affords the opportunity to directly observe the effect of metal ion size on corresponding coordination complexes.

Theoretical NMR Spectra. Theoretical NMR shielding constants in solution are known to be exceedingly difficult to calculate accurately.[48−51] Here, we achieved reasonably accurate results compared to experiment by computing NMR using DFT with the PBE0 hybrid exchange-correlation functional[52] and the pcSseg-3 basis set[53] for hydrogen atoms on a single energy-optimized reference geometry.

J-Coupling constants were not calculated. Chemical shifts were calculated with respect to an energy-optimized model tetramethylsilane (TMS) molecule at the same level of theory, surrounded by a shell of explicit water molecules. We found that the inclusion of a second shell of 12−17 explicit water molecules around the metal−ligand complex, in addition to a polarizable continuum model (PCM), improved the agreement between DFT-calculated and experimental NMRs compared with the PCM alone. This is presumably due to the improved

modeling of charge transfer effects to which NMR signals are highly sensitive.

By repeating calculations using different (energy-minimized) arrangements of water molecules around the metal–ligand complexes, we observed that the calculated chemical shifts of the aliphatic hydrogen atoms (which are no more than four bonds removed from H-bonding sites) depend quite strongly on the precise configuration, protonation state, and number of explicit water molecules in the second shell. On the one hand, this is in accordance with previous work that suggests a better agreement between theoretical and experimental NMR spectra can only be achieved by conformationally averaging calculated chemical shifts over a large sample of configurations with, for example, Monte Carlo or molecular dynamics approaches.[48,54−56] On the other hand, the calculated NMR chemical shifts of the aromatic hydrogen atoms in the nonpolar regions of the complexes, which agree best with experimental NMR chemical shifts, were found to depend only weakly on the metal–ligand complex configuration and arrangement of explicit water molecules and to depend moderately on the overall system charge.

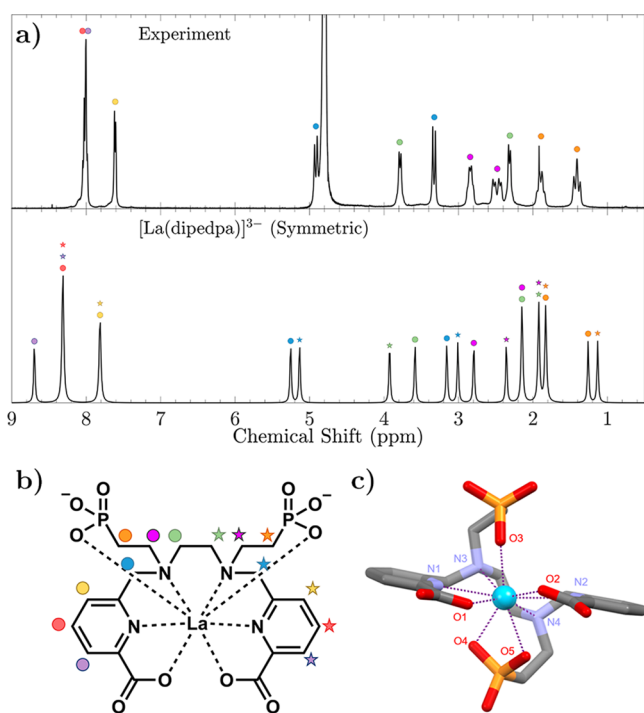In panel (a) of Figures 5–8, we present comparisons between experimental and DFT-calculated NMR spectra for

Figure 5. (a) Comparison of the experimental NMR of La(dipedpa) at pH 7 in D_2O and DFT-calculated NMR spectra of symmetrically coordinated $[La(dipedpa)]^{3-}$. (b) Corresponding NMR peak assignments. (c) DFT-optimized structure of $[La(dipedpa)]^{3-}$ with an explicit second shell of water molecules solvated in an H_2O-parametrized PCM. Ligand hydrogens and second-shell water molecules omitted for clarity.

the aforementioned complexes. The corresponding peak assignments are conveyed by the adjacent (b) panels. The protonation state selected for metal–ligand complexes in the theoretical NMR calculation was selected as the most abundant protonation state of the complexes found at the pH of the corresponding experimental NMR spectra, as determined by solution studies. Both symmetric and
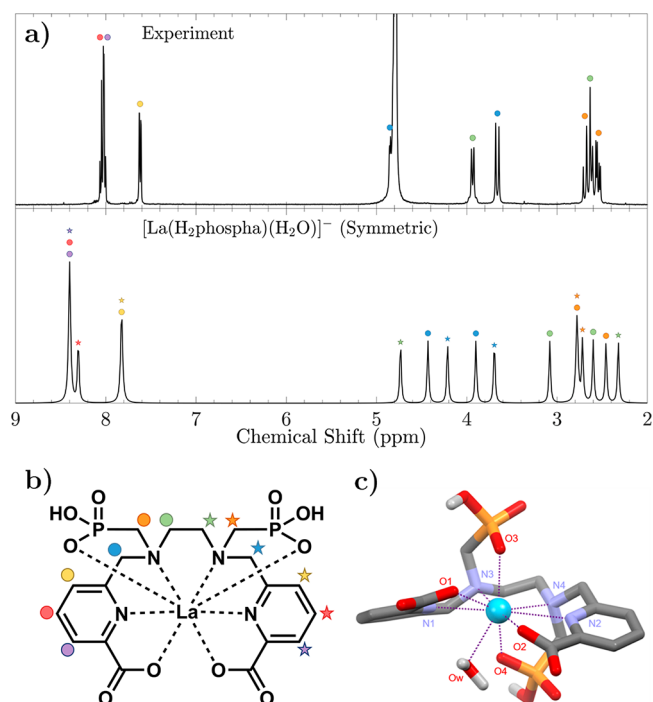

Figure 6. (a) Comparison of the experimental NMR of La(phospha) at pH 4 in D_2O and DFT-calculated NMR spectra of symmetrically coordinated $[La(H_2phospha)(H_2O)]^-$. (b) Corresponding NMR peak assignments. (c) DFT-optimized structure of $[La(H_2phospha)-(H_2O)]^-$ with an explicit second shell of water molecules solvated in an H_2O-parametrized PCM. Ligand hydrogens and second-shell water molecules omitted for clarity.
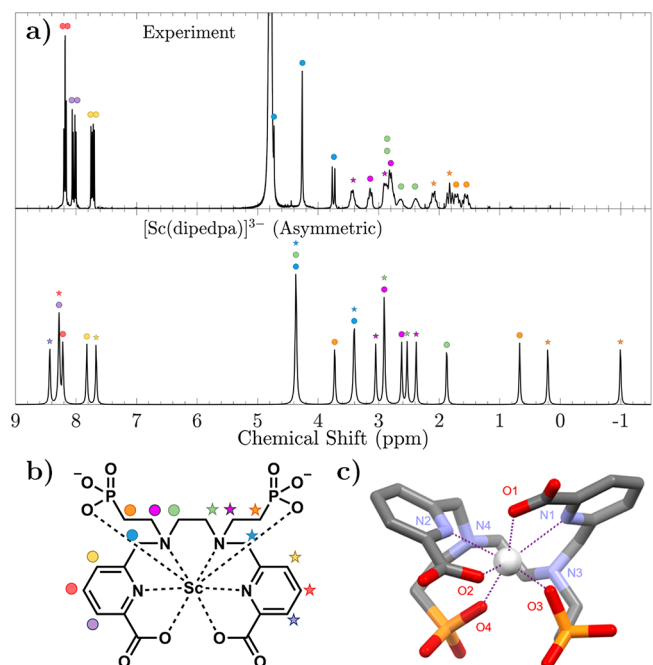

Figure 7. (a) Comparison of the experimental NMR of Sc(dipedpa) at pH 7 in D_2O and DFT-calculated NMR spectra of asymmetrically coordinated $[Sc(dipedpa)]^{3-}$. (b) Corresponding NMR peak assignments. (c) DFT-optimized structure of $[Sc(dipedpa)]^{3-}$ with an explicit second shell of water molecules solvated in an H_2O-parametrized PCM. Ligand hydrogens and second-shell water molecules omitted for clarity.

Figure 8. (a) Comparison of the experimental NMR of Sc(phospha) at pH 4 in D_2O and DFT-calculated NMR spectra of asymmetrically coordinated $[Sc(H_2phospha)]^-$. (b) Corresponding NMR peak assignments. (c) DFT-optimized structure of $[Sc(H_2phospha)]^-$ with an explicit second shell of water molecules solvated in an H_2O-parametrized PCM. Ligand hydrogens and second-shell water molecules omitted for clarity.
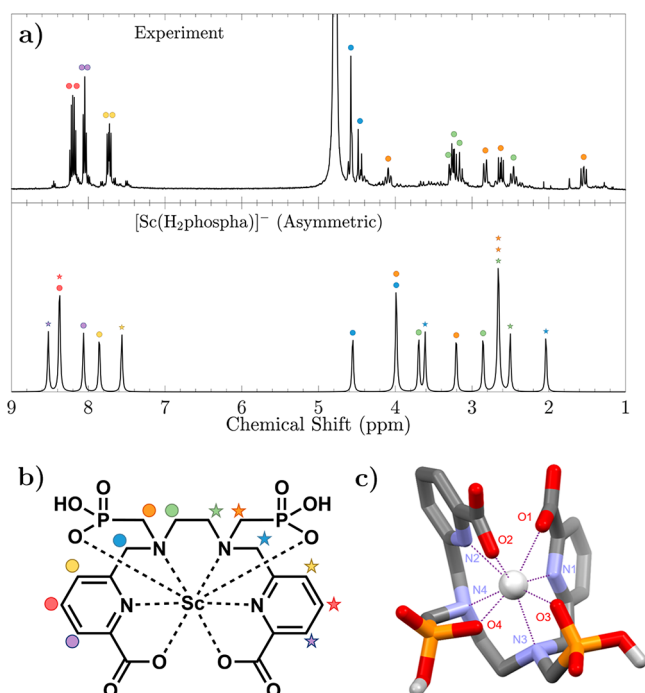
asymmetric ligand bonding patterns were tested in the case of the scandium complexes, but the resulting single-configuration theoretical aliphatic ^{1}H NMR chemical shifts are too imprecise compared with experiment to conclude if either is a better match (Figures S69 and S70). The DFT calculations, however, confirm that the Sc^{3+}-dipedpa and -phospha complexes are lower in energy when bound asymmetrically than symmetrically (see Table S7 for full DFT thermochemical results of the calculated Sc^{3+} and La^{3+} complexes).

From Figures 5–8 it is evident that calculated spectra of La^{3+} complexes are qualitatively in better agreement with experimental spectra than calculated spectra of Sc^{3+} complexes. We attribute this to the greater need for conformational averaging in the Sc^{3+} complexes caused by a less rigid chelation, which is due to the mismatch between the Sc^{3+} ion and the binding pocket sizes of $H_6phospha$ and $H_6dipedpa$.

DFT-Calculated Complexation Constants. Ligand–Metal stability constants are characterized by the equilibrium reaction given in eq 5. The stability constant is connected to the free energy difference between the reactants and products, which can be calculated theoretically. However, the theoretical prediction of ligand–metal binding free energies and complexation constants in solution is generally regarded as an exceedingly complicated problem requiring a rigorous calculation of thermodynamic variables, which is currently computationally intractable.[57,58] Assuming that accurate electronic structures can be calculated, sampling a sufficiently large number of thermodynamically important configurations of both reactants and products is a necessity, which includes the need to accurately account for the possible configurations of solvation shells and protonation states. A handful of recent

studies[57,59−62] have attempted to simplify the problem by assuming a single minimized energy reference conformation in both the reactants and products while ignoring possible effects from multiple protonation states, usually opting for a fully deprotonated structure with a PCM solvent model combined with two explicit solvation shells for the solvated metal ion. Although the resulting calculated stability constants are not generally in agreement with experiment, the errors are systematic and can be corrected by a simple linear correction to match experimental values.

The stability constant calculation method used here is similar to that discussed above but accounts for protonation states and opts for a higher-accuracy solvation model. Here, we calculate stability constants from free energies calculated via DFT by assuming a linear combination of reaction products with differing protonation states (eq 1), where G are the free energies, a are the

$$G_{product} = \sum_a x_a G[M(H_aL)(H_2O)_b]$$
(1)

protonation states with corresponding mole fraction x_a, and b varies (from 12−17) with each particular structure such that a full explicit second shell of H_2O is achieved in each case, and all possible hydrogen-bonding sites are quenched in the complex. Each structure is taken to be an energy-minimized configuration including an explicit second solvation shell in addition to the usual PCM. The protonation states of the reaction products depend on the pH of interest and are taken from solution studies (see Figure 3 for speciation plots). From this total free energy, we subtract the free energy of all acidic protons in the product complexes, which we model as a solvated proton in an energy-minimized cluster of 23 H_2O molecules. Additionally, the energy of all explicit water molecules must be subtracted from both the product and reactant sides, as they may not be equal in our model. The free energy of water was taken to be the average free energy per molecule of an energy-minimized cluster of 23 water molecules at the same level of theory. Hence, the net product free energy in our model is eq 2.

$$G_{product} = \sum_a x_a(G[M(H_aL)(H_2O)_b] - aG[H^+(H_2O)_c]) - (b - c)G[H_2O])$$
(2)

A pH-dependent mixture of free-ligand protonation states was also used to calculate reactant free energies. As for the products, all free ligands were solvated in an explicit shell (of 18−19) of water molecules in addition to the PCM, such that all H-bonding sites in the ligand were quenched. For each reactant, the energy of all labile protons and explicit solvent molecules was subtracted in order to balance the proton and water count on each side of the equation. The total free energy of reactants is then taken to be a linear combination of all protonation states, whose coefficients are simply the experimental mole fractions at a given pH (determined by the experimental pH corresponding to the metal complex of interest). Finally, the free metal ion was modeled with two explicit solvation shells of water, in addition to the PCM used to approximate the bulk effects of water. The total reactant free energy in our model is as in eq 3.

Table 3. Comparison of DFT-Calculated Equilibrium Constants for La^{3+} and Sc^{3+} phospa/dipedpa Complexes[a]

species	symmetry	log K (theory)	log K (experimental)	$\Delta(\Delta G_{rxn})$ (kJ/mol)
[La(H$_2$phospha)(H$_2$O)]$^-$	Symmetric	19.04	37.97 (3)	107.98
[La(Hphospha)(H$_2$O)]$^{2-}$	Symmetric	18.59	33.40 (1)	84.47
[Sc(H$_2$phospha)]$^-$	Symmetric	24.63	45.14 (4)	117.10
[Sc(H$_2$phospha)]$^-$	Asymmetric	26.64		105.68
[Sc(Hphospha)]$^{2-}$	Symmetric	26.86	40.86 (4)	79.98
[Sc(Hphospha)]$^{2-}$	Asymmetric	29.68		63.88
[La(dipedpa)]$^{3-}$	Symmetric	11.09	25.82 (3)	84.05
[Sc(dipedpa)]$^{3-}$	Symmetric	17.01	25.17 (3)	46.55
[Sc(dipedpa)]$^{3-}$	Asymmetric	18.58		37.59

[a]Structures calculated in H$_2$O-parametrized PCM with explicit second shell of water molecules. The final column lists the difference in reaction free energy between theoretical and experimental, $\Delta(\Delta G_{rxn}) = \Delta G_{rxn}(\text{DFT}) - \Delta G_{rxn}(\text{Experiment})$.

$$G_{reactant} = \sum_a x_a (G[(H_aL)(H_2O)_b] - aG[H^+(H_2O)_c]$$
$$- (b - c)G[H_2O]) + G[M^{3+}(H_2O)_d] - dG[H_2O] \tag{3}$$

From these free energies, the theoretical metal-complex formation constant is readily calculated as in eq 4.

$$\log K = \log(e^{-(G_{product} - G_{reactant})/RT}) \tag{4}$$

In all cases, the free energies are calculated by approximate thermodynamic corrections to the minimized potential energy, as produced automatically via a harmonic frequency calculation in Gaussian.[63] In Table 3, we compare the experimental and theoretical formation constants, as calculated by the model described above with T = 25.0 °C (298.15 K). These results highlight the inherent difficulty in obtaining accurate complexation constants. We found that our DFT-calculated formation constants are systematically lower than those of the experiment. We find (through a linear regression of theoretical vs experimental formation constants, R^2 = 0.67) that our DFT-calculated formation constants can be corrected to agree with experiment within 7.5 log K units by adding a systematic correction factor of b = 14.08 to the DFT-calculated values. No scaling is necessary, as the least-squares correlation slope m between theory and experiment was found to be near unity.

In the course of our research, we found that the calculated complexation constants are highly dependent on the particular arrangement of explicit water molecules surrounding the product complex. This is primarily because the geometry optimization procedure does not optimize for free energy. Instead, the potential energy is minimized. Consequently, it is challenging to obtain a representative sample of geometries with free energy minima from our existing structures. These low free energy configurations are the arrangements that must be sampled for an accurate estimate of the true free energy difference between reactants and products; thus, we hypothesize that an optimization of structures on the basis of lowest free energy, if possible, may ultimately lead to more accurate predictions of metal complex formation constants in the future.

Generally, denser and more ordered configurations of explicit water molecules have lower overall potential energies due to additional H bonding, but these states come at a significant zero-point vibrational energy "cost" due to the more rigid high-frequency vibrational modes. We found that the zero-point energy cost was significant enough to generally overcome any potential energy advantage imparted by a denser arrangement of water molecules with more H bonding. Hence, purposely arranging water molecules was futile, as more

randomly ordered explicit water shells were found to be lower in free energy. However, these randomly arranged water molecules impart a large uncertainty in the resulting calculated free energies, as the resulting free energy after optimization varies significantly. In summary, we find that our approach to the theoretical metal–ligand complexation constant calculation has intrinsic limits on its accuracy, which may go beyond the inherent accuracy of the underlying electronic structure theory. Accuracy beyond what is found here is unlikely to be obtained from sampling only a single energy-minimized configuration. The use of an algorithm to minimize free energy rather than potential energy may improve the accuracy, while sampling the free energy of an ensemble of configurations is likely required for high accuracy.

DFT-Optimized Complexes: Structural Features. As previously discussed, the most evident difference between La^{3+} and Sc^{3+} complexes of H$_6$phospa and H$_6$dipedpa is symmetry. As seen in panel (c) of Figures 5 and 6, the larger La^{3+} ion completely fills the binding pockets of H$_6$phospa and H$_6$dipedpa, resulting in a rigid, symmetric complex that, in the case of [La(H$_2$phospa)]$^-$, becomes coordinatively saturated upon inclusion of an explicit water molecule. We did not observe an additional water molecule to coordinate [La-(dipedpa)]$^{3-}$; instead, [La(dipedpa)]$^{3-}$ was found to exhibit a coordination of two oxygen atoms from one of the phosphate groups, which was not observed for [La(H$_2$phospha)]$^-$. Conversely, the smaller Sc^{3+} ion is too small to accommodate the typical twisted picolinic acid binding motif of many pa family ligands and, as such, conforms to an asymmetric configuration, where pyridine rings coordinate perpendicular to one another, and phosphonate arms lie uncharacteristically adjacent. No water coordination is possible in [Sc-(H$_2$phospa)]$^-$ due to the small metal ion size and coordination requirements of Sc^{3+}. Despite its structural differences with [La(H$_2$phospa)(H$_2$O)]$^-$, [Sc(H$_2$phospa)]$^-$ is also rigid in solution, as evinced by the peaks in the ^{1}H NMR spectrum. Analysis of the DFT-optimized bond lengths presented in Table S10 reveals predictably longer bond lengths for the La^{3+} complex as a consequence of its larger ionic radii. Surprisingly, despite the asymmetric conformation of the Sc^{3+} complex, bond distances of identical functional groups (e.g., **N1** vs **N2**) are uniform, except in [Sc(dipedpa)]$^{3-}$. For both complexes, coordinating phosphonate bonds are the shortest, followed sequentially by pyridine amines, picolinates, and backbone tertiary amines.

CONCLUSIONS

H$_6$phospa, H$_6$dipedpa, and H$_6$eppy were successfully synthesized and fully characterized. X-ray quality crystals of H$_6$phospa and H$_6$dipedpa further confirmed the characterization and, in the former case, revealed intramolecular hydrogen bonding. Metal ion chelation was studied by NMR (^{1}H, ^{31}P{^{1}H}) spectroscopy and ^{1}H$-^1$H COSY. Picolinic acid bearing ligands were determined to form rigid, symmetric complexes with La^{3+} and rigid, asymmetric complexes with Sc^{3+}. This tendency was not observed with H$_6$eppy. Instead a rigid, symmetric complex was observed with Sc^{3+}, and broad peaks were noted in the ^{1}H NMR spectrum with La^{3+}. Solution studies (potentiometric, spectrophotometric) were conducted to determine the protonation constants of each ligand. The most basic pK_a of H$_6$phospa was validated by ^{31}P{^{1}H} and ^{1}H NMR titrations. Thermodynamic stabilities of each ligand with In^{3+}, Y^{3+}, Sc^{3+}, Lu^{3+}, and La^{3+} were determined; in each case, speciation diagrams and pM values were calculated. In general, H$_6$phospa produced the most stable complexes, and H$_6$eppy made the least stable complexes. Moreover, In^{3+} complexes were the most stable, and the La^{3+} complexes were the least stable. Structures of La^{3+} and Sc^{3+} complexes of H$_6$phospa and H$_6$dipedpa were calculated. The symmetry of calculated complexes is consistent with observations from NMR spectra. To further validate the data, NMR spectra and equilibrium constants of La^{3+}/Sc^{3+} H$_6$phospha and H$_6$dipedpa complexes were generated from DFT-optimized structures and compared to experimental spectra. The number of explicit water molecules, protonation states, and configurations were varied in an attempt to discern their importance for modeling these coordination complexes. The models with the most explicit water molecules were observed to qualitatively fit the experimental data best, although a strong free energy and NMR shielding constant dependence on the exact arrangement of explicit water molecules was observed. We hypothesize that a better accuracy in the calculation of theoretical metal–ligand complexation constants and proton NMR shielding constants is likely to require configurational averaging in some way, or possibly a free energy minimization scheme to properly sample the most important configurations of both the reactants and products.

EXPERIMENTAL SECTION

Materials and Methods. All solvents and reagents were purchased from commercial suppliers (Sigma-Aldrich, Fisher Scientific, TCI America, Alfa Aesar, AK Scientific, Fluka) and were used as received. Synthetic reactions were monitored by thin-layer chromatography (TLC) (MERCK Silicagel 60 F254, aluminum sheet). Flash chromatography was performed using Redisep Rf high performance (HP) silica columns and a Teledyne Isco Combiflash Rf automated system. Water was ultrapure (18.2 MΩ cm^{-1} at 25 °C, Milli-Q, Millipore). ^{1}H, ^{13}C{^{1}H}, and ^{31}P{^{1}H} NMR spectra were recorded at ambient temperature on Bruker AV300 and AV400 instruments; unless otherwise specified, the NMR spectra are expressed on the δ scale and referenced to residual solvent peaks. LR-ESI-MS was performed using a Waters ZG spectrometer with an electrospray chemical ionization (ESCI) source, and HR-ESI-MS was performed on a Micromass LCT time-of-flight instrument at the Department of Chemistry, University of British Columbia. Microanalyses for C, H, and N were performed on a Carlo Erba elemental analyzer EA 1108.

Synthesis and Characterization. *Dimethyl-6,6′-([ethane-1,2-diylbis{azanediyl}]bis[methylene])dipicolinate (1).* Compound **1** was prepared according to the literature with appropriate characteristic spectra.[33]

H$_6$phospa (2). Compound **2** was prepared according to the literature with appropriate characteristic spectra.[32] HR-ESI-MS calcd for $[C_{18}H_{24}N_4O_{12}P_2 + K]^+$: 557.0605; found $[M + K]^+$ = 557.0601. Elemental analysis: calcd% for H$_6$phospa·0.3HCl·1.8H$_2$O: C 38.55, H 5.00, N 9.99; found: C 39.03, H 4.95, N 9.78.

H$_6$dipedpa (3). Compound **1** (400 mg, 1.12 mmol) was added to a stirring solution of deionized water (diH$_2$O, 4 mL) in a 10 mL round-bottom flask, and the solution pH was adjusted to 9−10 (measured by pH paper) with 1 M NaOH. Compound **1** was observed to dissolve only above ∼pH 7. Diethyl vinylphosphonate (720 μL, 769 mg, 4.68 mmol) was added to the stirring aqueous solution, after which point the solution was heated to reflux and left to stir overnight. Following a confirmation of the desired intermediate (double Michael-addition product) by mass spectrometry, the solution was cooled and extracted with dichloromethane (DCM) (5 mL × 3) in a separatory funnel to remove excess diethyl vinylphosphonate. The aqueous phase was evaporated, and upon drying, conc HCl (6 mL) was added to the resultant oil. The solution was refluxed and stirred overnight. The solution was allowed to cool to ambient temperature (precipitate was noted following the cooling), and the HCl was evaporated in vacuo. Residual HCl was removed by repeatedly adding H$_2$O (10 mL × 3) and evaporating to near-dryness. To the residual water, acetone (15 mL) was added, at which point a fine light brown colored precipitate formed. After it sat untouched for 30 min, the fine precipitate formed small droplets of an oil-like liquid along the sides and bottom of the flask. The acetone solution was decanted, and the oil was washed with acetone and filtered to yield a fine white powder. The acetone solution was evaporated, and the process was repeated twice or thrice until the purity of the product declined (18%, 145.7 mg, 0.20 mmol). ^{1}H NMR (400 MHz, D$_2$O, 25 °C): δ 7.84 (t, J = 7.7 Hz, 1H), 7.80 (d, J = 7.6 Hz, 1H), 7.44 (d, J = 7.3 Hz, 1H), 4.20 (s, 2H), 3.29 (s, 2H), 3.25 (m, 2H), 1.98 (m, 2H). ^{13}C{^{1}H} NMR (75 MHz, D$_2$O, 25 °C): δ 172.2, 152.7, 138.7, 125.5, 123.3, 51.6, 48.8, 25.0, 23.7. ^{31}P{^{1}H} NMR (162 MHz, D$_2$O, 25 °C): 19.07. HR-ESI-MS calcd for $[C_{20}H_{28}N_4O_{12}P_2 + H]^+$: 547.1359; found $[M + K]^+$ = 547.1362. Elemental analysis: calcd% for H$_6$dipedpa·4HCl·2H$_2$O: C 32.94, H 4.99, N 7.68; found: C 32.92, H 5.09, N 7.56.

Methyl-6-bromomethylpicolinate (4). Compound **4** was prepared according to the literature with appropriate characteristic spectra.[64]

Methyl 6-((diethoxyphosphoryl)methyl)picolinate (5). To a solution of (**4**) (1.5 g, 6.52 mmol) in acetonitrile (ACN) (100 mL) in a 250 mL round-bottom flask was added P(OEt)$_3$ (2.85 mL, 16.6 mmol) and ZnBr$_2$ (0.44 g, 1.96 mmol). The reaction mixture was heated to 60 °C and stirred for 48 h and monitored by TLC (DCM, 10% MeOH) until completion. The reaction mixture was quenched with distilled water and extracted with DCM (4 × 100 mL); the organic layers were combined and dried over anhydrous MgSO$_4$. After filtration, the crude product was adsorbed to silica and purified by silica chromatography (CombiFlash Rf automated column system 40 g of HP silica; solid (pause) preparation; A: DCM, B: MeOH, 100% A to 20% B, to yield a semipure product (yield over two reactions shown in the next step). ^{1}H NMR (300 MHz, CDCl$_3$, 25 °C): δ 8.04 (d, 1H), 7.84 (t, 1H), 7.66 (d, 1H), 4.17−4.05 (m, 4H), 4.00 (s, 3H), 3.60 (d, 2H), 1.27 (t, 6H). LR-ESI-MS calcd for $[C_{12}H_{18}NO_5P + Na]^+$: 310.0; found $[M + H]^+$ = 310.1.

Diethyl ((6-(hydroxymethyl)pyridin-2-yl)methyl)phosphonate (6). To a solution of (**5**) (1.69 g, 5.9 mmol) in a mixture of 7:3 DCM/MeOH (100 mL) in a 250 mL round-bottom flask at 0 °C was added NaBH$_4$ (0.27 g, 7.1 mmol) over 1 h. The reaction mixture was stirred, allowed to warm to room temperature, and left to react overnight (∼16 h). It was then quenched with distilled water, and the phases were separated; the aqueous phase was evaporated to remove MeOH. The residue was then washed with DCM (3 × 100 mL), and the organic phases were then combined and dried over anhydrous MgSO$_4$. After a filtration, the crude product was adsorbed to diatomaceous earth and purified by silica chromatography (Combi-Flash Rf automated column system 40 g HP silica; solid (pause) preparation; A: DCM, B: MeOH, 100% A to 25% B, to yield the pure product (58% over two steps, 0.98 g). ^{1}H NMR (400 MHz, CDCl$_3$, 25 °C): δ 7.62 (t, J = 7.7 Hz, 1H), 7.28−7.22 (m, 1H), 7.15 (d, J =

7.3 Hz, 1H), 4.70 (s, 2H), 4.05 (dq, $J = 8.2, 7.1$ Hz, 4H), 3.40 (d, $J = 22.0$ Hz, 2H), 1.24 (t, $J = 7.1$ Hz, 6H). $^{13}C\{^1H\}$ NMR (101 MHz, CDCl$_3$, 25 °C): 159.2 (d, $J = 2.4$ Hz), 151.7 (d, $J = 8.4$ Hz), 137.4 (d, $J = 2.7$ Hz), 122.9 (d, $J = 5.3$ Hz), 118.8 (d, $J = 3.3$ Hz), 64.0, 62.4 (d, $J = 6.6$ Hz), 36.4 (d, $J = 135.7$ Hz), 16.5 (d, $J = 6.1$ Hz). $^{31}P\{^1H\}$ NMR (162 MHz, CDCl$_3$, 25 °C, externally referenced to 85% phosphoric acid): 23.08. LR-ESI-MS calcd for $[C_{11}H_{18}NO_4P + Na]^+$: 282.1; found $[M + Na]^+ = 282.2$.

Diethyl ((6-(bromomethyl)pyridin-2-yl)methyl)phosphonate (7). To a solution of (**6**) (0.35 g, 1.35 mmol) in ACN (20 mL) in a 50 mL round-bottom flask at 0 °C was added PBr$_3$ (0.13 mL, 1.35 mol) dropwise. The reaction mixture was stirred, allowed to warm to room temperature, and monitored by TLC (DCM, 10% MeOH). After 3 h, the reaction mixture was quenched with dilute NaHCO$_3$ and extracted with DCM (4 × 20 mL). The organic phases were combined and dried over anhydrous MgSO$_4$. Filtration and evaporation yielded the pure product (85%, 0.37 g). *Note! Product prone to decomposition—use immediately or refrigerate and use within 48 h.* ^1H NMR (400 MHz, CDCl$_3$, 25 °C): δ 7.64 (t, $J = 7.7$ Hz, 1H), 7.36−7.27 (m, 2H), 4.51 (s, 2H), 4.08 (dq, $J = 7.2$ Hz, 4H), 3.40 (d, $J = 22.0$ Hz, 2H), 1.26 (t, $J = 7.0$ Hz, 6H). $^{13}C\{^1H\}$ NMR (101 MHz, CDCl$_3$, 25 °C) 156.5 (d, $J = 2.5$ Hz), 152.8 (d, $J = 8.2$ Hz), 137.6 (d, $J = 2.7$ Hz), 123.6 (d, $J = 4.8$ Hz), 121.7 (d, $J = 3.1$ Hz), 62.3 (d, $J = 6.5$ Hz), 36.5 (d, $J = 134.7$), 33.8, 16.4 (d, $J = 6.2$ Hz). $^{31}P\{^1H\}$ NMR (162 MHz, CDCl$_3$, 25 °C, externally referenced to 85% phosphoric acid): 24.53. LR-ESI-MS calcd for $[C_{11}H_{18}BrNO_3P + H]^+$: 322.0; found $[M + H]^+ = 322.1$

Ethylenediaminediacetic Acid Dimethyl Ester Dihydrochloride (8). Thionyl chloride (6.2 mL, 56.8 mmol) was slowly added to MeOH (150 mL) at 0 °C in a 500 mL round-bottom flask and was allowed to stir for 30 min. Ethylenediaminediacetic acid (5.00 g, 28.4 mmol) was then added, and the reaction mixture was heated to reflux for 24 h. Solvent was then evaporated, and the crude product washed twice with hexanes to remove residual HCl. The resulting solid was recrystallized in MeOH to yield the pure product as the dihydrochloride salt (80%, 6.27 g, 22.6 mmol). ^1H NMR (400 MHz, D$_2$O, 25 °C): δ 4.04 (s, 2H), 3.77 (s, 3H), 3.50 (s, 2H). $^{13}C\{^1H\}$ NMR (100 MHz, 25 °C, D$_2$O + NaOD): 167.5, 53.7, 47.7, 42.9. LR-ESI-MS calcd for $[C_8H_{16}N_2O_4 + H]^+$: 205.1; found $[M + H]^+ = 205.3$ Elemental analysis: calcd% for C$_{16}$H$_{20}$N$_2$·2HCl: C 61.4, H 7.08, N 8.94; found: C 61.67, H 6.95, N 8.94.

Dimethyl 2,2'-(ethane-1,2-diylbis(((6-((diethoxyphosphoryl)-methyl)pyridin-2-yl)methyl)-azanediyl))diacetate (9). To a solution of (**8**) (0.2 g, 0.62 mmol) in ACN (5 mL) in a 20 mL conical vial was added Na$_2$CO$_3$ (0.1 g, 1.2 mmol). The solution was stirred and heated to 40 °C before the slow addition of (**9**) (65 mg, 0.27 mmol). The reaction was allowed to proceed for 3 d and monitored by LR-ESI-MS. Upon completion, the reaction mixture was washed with water to remove salt and extracted with DCM (3 × 20 mL). The organic phases were combined and dried over anhydrous MgSO$_4$. After filtration, the product was absorbed to diatomaceous earth and purified by silica chromatography (CombiFlash Rf automated column system) with 12 g of HP silica; solid (pause) preparation; A: DCM, B: MeOH, 100% A to 20% B, to yield the pure product (42%, 78 mg). ^1H NMR (400 MHz, CDCl$_3$, 25 °C): δ 7.56 (br s, 1H), 7.32−7.28 (br m, 1H), 7.21 (d, 1H) 4.02 (m, 4H), 3.89 (s, 2H), 3.63 (s, 3H), 3.42−3.35 (m, 4H), 2.84 (s, 2H) 1.21 (t, 6H). $^{13}C\{^1H\}$ NMR (101 MHz, CDCl$_3$, 25 °C): 171.7, 158.8, 152.0, 137.0, 122.6, 121.1, 62.2 (d, $J_1^{PC} = 6.5$ Hz), 60.0, 54.9, 52.2, 51.4, 37.0, 36.3 (d, $J_1^{PC} = 136.0$ Hz), 16.3 (d, $J_2^{PC} = 6.2$ Hz). $^{31}P\{^1H\}$ NMR (162 MHz, CDCl3, 25 °C): 25.8. LR-ESI-MS calcd for $[C_{30}H_{48}N_4O_{10}P_2 + Na]^+$: 709.3; found $[M + Na]^+ = 709.3$

H$_6$eppy (10). To conc HCl (5 mL) in a 20 mL conical vial was added (**9**) (78 mg, 0.11 mmol), which was stirred and heated at reflux for 48 h. The solvent was then evaporated, and the product was dissolved in a minimal amount of water. Next, acetone was added to the solution, forming a slurry of white solid as well as a sticky oil. The mixture was allowed to sit for 30 min and then decanted and dried under reduced pressure to yield the pure product (75%, 47 mg). ^1H NMR (300 MHz, D$_2$O, 25 °C): 8.30 (t, 1H), 7.80 (m, 2H), 4.50 (s,

2H) 3.83 (s, 2H), 3.53 (d, 2H), 3.42 (s, 2H). $^{13}C\{^1H\}$ NMR (75 MHz, D$_2$O, 25 °C): 171.8, 152.3, 148.7, 145.5, 127.6, 127.6, 125.4, 55.6, 54.4, 51.4, 35.5, 34.3. $^{31}P\{^1H\}$ NMR (120 MHz, CDCl$_3$, 25 °C): 14.7 (s). HR-ESI-MS: calcd for $[C_{20}H_{28}N_4O_{10}P_2 + H]^+$: 547.1359; found: 547.1360. Elemental analysis: calcd% for H$_6$eppy·4.5HCl·3H$_2$O: C 31.38, H 5.10, N 7.32; found: C 31.46, H 5.19, N 7.22.

Metal Complexation. NMR spectra of H$_6$phospa, H$_6$dipedpa, and H$_6$eppy complexes with In^{3+}, Lu^{3+}, Y^{3+}, Sc^{3+}, and La^{3+} were obtained by making separate ligand and metal solutions in D$_2$O (16 mM) and then mixing the given ligand (L) solution with a given metal (M) solution in a molar ratio of 1:1.1 L/M ($V_t = 525$ μL). If necessary, the solution pD was altered with freshly prepared ~0.1 M and/or 1 M NaOD (diluted from 40 wt % NaOD) and measured with a Ross combined electrode and corrected pD = pH$_{measured}$ + 0.4. Solutions were allowed to stand for at least 15 min at room temperature before NMR spectra were collected. Complexation was also confirmed by HR-ESI-MS (see Table S11).

X-ray Crystallography. Single white needle-shaped crystals of H$_6$phospa (**2**) and H$_6$dipedpa (**3**) were obtained by a recrystallization from a slow evaporation of acetone into ligand solution. Suitable crystals 0.03 × 0.01 × 0.001 mm^3 and 0.01 × 0.01 × 0.001 mm^3 (respectively) were selected and mounted on a suitable support on a Bruker APEX II area detector diffractometer. The crystal was kept at a steady $T = 90$ K during the data collection. The structure was solved with the ShelXT[65] structure solution program using the Intrinsic Phasing solution method and by using Olex2[66] as the graphical interface. The model was refined with version 2018/1 of ShelXL[65] using a least-squares minimization.

Solution Thermodynamics. In general, aqueous metal−ligand systems and their cumulative stability constants, defined by the associations $\beta(M_pH_qL_r)$ (e.g., ligand species H$_q$L, metal complexes species M$_p$H$_q$L$_r$, and metal hydrolysis species M$_p$H$_q$), can be defined by eq 5, where M is the metal ion, L is the fully deprotonated chelating ligand, and p, q, and r are the stoichiometric numbers of the components.[67]

$$p\text{M} + q\text{H} + r\text{L} \leftrightarrow \text{M}p\text{H}q\text{L}r$$
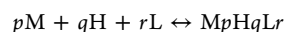
$$\beta(M_pH_qL_r) = [M_pH_qL_r]/[M]_p[H]_q[L]_r \tag{5}$$

Protonation constants were calculated with HypSpec2014,[44] HypNMR2008,[43] and HyperQuad2013[45] software and are presented in Table 1.

All combined UV-potentiometric titrations were performed in a 20 mL 25 °C thermostated glass cell with an inlet−outlet tube for nitrogen gas (purified through a 10% NaOH solution to exclude CO$_2$ prior to and during the course of the titration). The titration apparatus comprised a Metrohm Titrando 809, a Metrohm Dosino 800 equipped with a Ross combined electrode, and an optic dip probe (0.2 cm) connected to a Varian Cary 60 UV/vis spectrophotometer (200−400 nm). The electrode was calibrated daily in a hydrogen ion concentration by direct titration of HCl with freshly prepared NaOH solution, and the results were analyzed with the Gran procedure[68] in order to obtain the standard potential ($E°$) and the ionic product of water pK_w, with $T = 25$ °C and 0.16 M NaCl as a supporting electrolyte. Solutions were titrated with carbonate-free NaOH (~0.16 M) that was standardized against freshly recrystallized potassium hydrogen phthalate. Each titration consisted of 100−150 equilibrium points in the pH range of 1.8−11.5; equilibration times for titrations were 2 min for pK_a titrations and up to 5 min for metal complex titrations. Protonation equilibria of the ligands (H$_6$L = H$_6$phospa, H$_6$dipedpa, and H$_6$eppy) were studied by combined UV-potentiometric titrations of solutions containing the ligands ([H$_6$phospa] = 4.84 × 10^{-4} M, [H$_6$dipedpa] = 6.76 × 10^{-4} M and [H$_6$eppy] = 7.15 × 10^{-4} M) at $T = 25$ °C, $l = 0.2$ cm, and 0.16 M NaCl ionic strength in the pH range of 1.8−11.5. The most acidic protonation constants corresponding to a phosphonate functionality were determined by acidic UV-batch experiments ($l = 1$ cm). The H$^+$ concentration in this UV in-batch titration procedure at low pH solutions ($0 \leq$ pH ≤ 2) was calculated from solution stoichiometry, not measured with a glass electrode, and the correct acidity scale H^0 was used.[69] In-batch

solutions were prepared by adding to the ligand solutions and standardized HCl and NaCl to set the ionic strength constant at 0.16 M when possible.

All the spectrophotometric and potentiometric data were analyzed with HypSpec2014[44] and HyperQuad2013[45] to obtain the protonation constants in Table 1. Additional ^{31}P and ^{1}H NMR titrations were employed to determine the most acidic protonation constant (P−OH) and more basic pK_a (N_{en}) in H_6phospa. NMR data were processed using the HypNMR[43] software.

Complex formation equilibria of H_6phospa, H_6dipedpa, and H_6eppy with the metal ions In^{3+}, Sc^{3+}, Y^{3+}, Lu^{3+}, and La^{3+} were studied by two different methods. The first method used UV−vis batch spectrophotometric measurements ($l = 1$ cm) on a set of solutions containing a 1:1 metal-to-ligand molar ratio ([H_6phospa] = 7.44×10^{-5} M and $M^{3+} = In^{3+}$, Sc^{3+}, Y^{3+}, Lu^{3+}, La^{3+}; [H_6dipedpa] = 7.10×10^{-5} M and $M^{3+} = In^{3+}$; [H_6eppy] = 7.32×10^{-5} M and $M^{3+} = In^{3+}$) and different amounts of standardized HCl and NaCl to set the ionic strength constant at 0.16 M when possible. The molar absorptivities of all the protonated species of each of the ligands calculated with HypSpec2014[44] from the protonation constant experiments described above were included in the calculations of the metal complexes. The second method as in the case of protonation constants was combined UV-potentiometric titrations (25 °C, $I = 0.16$ M NaCl and $l = 0.2$ cm). Ligands and metal concentrations were in the range of $(4.05−5.9) \times 10^{-4}$ M. M^{3+} metal ion solutions were prepared by adding the atomic absorption (AA) standard solution to each of the different ligands of known concentration in the 1:1 metal-to-ligand molar ratio. The exact amount of acid present in the AA standard solution was determined by the Gran method[68] titrating equimolar solutions of M^{3+} and Na_2H_2-ethylenediamine tetraacetic acid (EDTA). Each titration consisted of 100−150 equilibrium points in the pH range of 1.6− 11.5; the equilibration time for titrations was up to 5 min for metal complex titrations. Three replicates of each titration were performed. Relying on the stability constants for the species $M(H_3L)$ obtained by the acidic batch method, the fitting of the direct potentiometric titrations was possible yielding the stability constants in Table 2. All the potentiometric measurements were processed using the Hyperquad2013 software,[45] while the obtained spectrophotometric data were processed with the HypSpec2014[44] program. Proton dissociation constants corresponding to the hydrolysis of M(III) aqueous ions included in the calculations were taken from Baes and Mesmer.[70] The overall equilibrium (formation) constants log β referred to the overall equilibria: $pM + qH + rL \leftrightarrows M_pH_qL_r$ (charges omitted), where p might also be 0 in the case of protonation equilibria, and q can be negative for metal-hydroxo species. Stepwise equilibrium constants log K correspond to the difference in log units between the overall constants of sequentially protonated (or hydroxo) species. The most useful parameter used to calculate the metal scavenging ability of a ligand toward a metal ion, pM, is defined as $-\log [M^{n+}]_{free}$ at [ligand] = 10 μM and $[M^{n+}] = 1$ μM at pH = 7.4.[47]

DFT Calculations. All DFT calculations were performed using Gaussian 16 rev. c01.[71] Self-consistent field (SCF) convergence criteria were set to their default values (SCF = Tight in Gaussian). Structure optimizations were performed without symmetry constraints using the Berny algorithm[72] with default settings, starting from initial structures built manually. Each structure was optimized, and free energies were calculated, using DFT with the PBE0 hybrid exchange-correlation functional,[52] added D3(BJ)[73−75] dispersion corrections, and the def2-TZVP basis set[76] for all nonmetal atoms. Effective core potentials (ECPs) were used to account for scalar relativistic effects in metal core electrons. Specifically, the Stuttgart relativistic small core (RSC) 1997 ECP basis set[77,78] was used for scandium atoms, while the Stuttgart RSC segmented valence basis set and ECP[79,80] were used for lanthanum. These metal basis sets were also used in NMR shielding calculations. Metal basis sets were downloaded from the Basis Set Exchange Web site.[81−83] The PBE0 functional was chosen due to its previous success in structure prediction and thermochemistry of transition-metal complexes,[84−88] while the def2-TZVP basis was chosen as a reasonable trade-off

between speed and accuracy for the large system sizes under study.[89,90] A local minimum of energy was confirmed after each optimization via a harmonic frequency analysis using analytical second derivatives, which also yields calculated thermochemical variables under standard-state conditions (25 °C, 1 atm). The integral equation formalism of the polarizable continuum model (IEFPCM) was used as an implicit water model in all calculations to simulate the average bulk dielectric effects of the solvent. Default IEFPCM parameters were used, as implemented in Gaussian ($\varepsilon = 78.36$, van der Waals surface without added spheres). Initially, each calculation was repeated with 0, 6, 9, and 12 explicit water molecules, which were placed randomly by the PACKMOL code[91] in a sphere up to 4.5 Å from the center of mass of each system. Adjustments were then made before optimization to move the randomly placed water molecules closer to hydrogen-bond centers, such as phosphonate and carboxyl groups. In revised calculations, 12−19 water molecules were placed deliberately around all hydrogen-bonding sites until all possible ligand hydrogen bonds were fully saturated with explicit water molecules— we consider this a full "second shell" of water molecules. ^{1}H NMR isotropic shielding constant calculations were performed on the revised, fully optimized structures using DFT with the gauge-including atomic orbital (GIAO) method[92,93] and PBE0 functional, as it has also been shown to perform well for the calculation of ^{1}H NMR shielding constants.[49,51,94] The choice of basis set is extremely important for the calculation of accurate NMR shielding constants, especially on the atoms of interest and those directly bound. Hence, we adopted the "locally dense" approach[95] for the calculation of ^{1}H NMR shielding constants by utilizing the pcSseg-3 basis set[53] (quadruple-ζ valence quality) on H atoms within the ligand and on any atom directly bound to ligand H atoms. Any atom two bonds away from a ligand H atom was given the smaller pcseg-2 basis set,[96] and all remaining atoms (including solvent atoms but not metal atoms) were given the pcseg-1 basis set. Calculation results were visualized and interpreted using GaussView version 6.0.[97]

■ ASSOCIATED CONTENT

Ⓢ Supporting Information

The Supporting Information is available free of charge at https://pubs.acs.org/doi/10.1021/acs.inorgchem.1c00290.

> Representative spectra of the in-batch UV titrations of $M^{3+}L$ (M = In, Lu, Sc, Y, La; L = phospa, dipedpa, eppy) systems as the pH is raised; stepwise protonation constants (log K) of $M^{3+}L$ (M = In, Lu, Sc, Y, La; L = phospa, dipedpa, eppy) complexes; NMR spectra (^{1}H, [31]P{^{1}H}, ^{13}C{^{1}H}, [1]H−^{1}H COSY) and high-resolution mass spectra of relevant synthetic intermediates, products, and metal complexes; X-ray crystal data of H_6phospa and H_6dipeda; DFT-calculated structures and theoretical NMR spectra of $M^{3+}L$ (M = La, Sc; L = phospa, dipedpa); data extracted from DFT structures used for calculation of theoretical log K values (PDF)

Accession Codes

CCDC 2034415−2034416 contain the supplementary crystallographic data for this paper. These data can be obtained free of charge via www.ccdc.cam.ac.uk/data_request/cif, or by emailing data_request@ccdc.cam.ac.uk, or by contacting The Cambridge Crystallographic Data Centre, 12 Union Road, Cambridge CB2 1EZ, UK; fax: +44 1223 336033.

■ AUTHOR INFORMATION

Corresponding Authors

María de Guadalupe Jaraquemada-Peláez − *Medicinal Inorganic Chemistry Group, Department of Chemistry, University of British Columbia, V6T 1Z1 Vancouver, British*

Columbia, Canada; ● orcid.org/0000-0002-6204-707X;
Email: mdgjara@chem.ubc.ca

Chris Orvig − *Medicinal Inorganic Chemistry Group,
Department of Chemistry, University of British Columbia,
V6T 1Z1 Vancouver, British Columbia, Canada;*
● orcid.org/0000-0002-2830-5493; Email: orvig@
chem.ubc.ca

Authors

Thomas I. Kostelnik − *Medicinal Inorganic Chemistry Group,
Department of Chemistry, University of British Columbia,
V6T 1Z1 Vancouver, British Columbia, Canada; Life
Sciences Division, TRIUMF, V6T 2A3 Vancouver, British
Columbia, Canada*

Hayden Scheiber − *Department of Chemistry, University of
British Columbia, V6T 1Z1 Vancouver, British Columbia,
Canada*

Rosita Cappai − *Medicinal Inorganic Chemistry Group,
Department of Chemistry, University of British Columbia,
V6T 1Z1 Vancouver, British Columbia, Canada;
Dipartimento di Scienze della Vita e dell'Ambiente,
University of Cagliari, 09042 Cagliari, Italy*

Neha Choudhary − *Medicinal Inorganic Chemistry Group,
Department of Chemistry, University of British Columbia,
V6T 1Z1 Vancouver, British Columbia, Canada; Life
Sciences Division, TRIUMF, V6T 2A3 Vancouver, British
Columbia, Canada*

Felix Lindheimer − *Medicinal Inorganic Chemistry Group,
Department of Chemistry, University of British Columbia,
V6T 1Z1 Vancouver, British Columbia, Canada;
Anorganisch-Chemisches Institut, Universität Heidelberg,
69120 Heidelberg, Germany*

Complete contact information is available at:
https://pubs.acs.org/10.1021/acs.inorgchem.1c00290

Author Contributions

The manuscript was written through contributions of all
authors. All authors have given approval of the final version of
the manuscript.

Notes

The authors declare no competing financial interest.

■ REFERENCES

(1) Kostelnik, T. I.; Orvig, C. Radioactive Main Group and Rare
Earth Metals for Imaging and Therapy. *Chem. Rev.* **2019**, *119*, 902−
956.

(2) Boros, E.; Packard, A. B. Radioactive Transition Metals for
Imaging and Therapy. *Chem. Rev.* **2019**, *119*, 870−901.

(3) Pinto, S. M.; Tomé, V.; Calvete, M. J. F.; Castro, M. M. C. A.;
Tóth, É.; Geraldes, C. F. G. C. Metal-Based Redox-Responsive MRI
Contrast Agents. *Coord. Chem. Rev.* **2019**, *390*, 1−31.

(4) Weekes, D. M.; Orvig, C. Harnessing the Bone-Seeking Ability of
Ca(II)-like Metal Ions in the Treatment of Metastatic Cancer and
Resorption Disorders. *Chem. Soc. Rev.* **2016**, *45*, 2024−2031.

(5) Lawson, M. K.; Valko, M.; Cronin, M. T. D.; Jomová, K.
Chelators in Iron and Copper Toxicity. *Curr. Pharmacol. Reports*
2016, *2*, 271−280.

(6) Bjørklund, G.; Mutter, J.; Aaseth, J. Metal Chelators and
Neurotoxicity: Lead, Mercury, and Arsenic. *Arch. Toxicol.* **2017**, *91*,
3787−3797.

(7) Di, Y.; Wasan, E. K.; Cawthray, J.; Syeda, J.; Ali, M.; Cooper, D.
M. L.; Al-Dissi, A.; Ashjaee, N.; Cheng, W.; Johnston, J. Evaluation of
La(XT), a Novel Lanthanide Compound, in an OVX Rat Model of
Osteoporosis. *Bone Rep.* **2021**, *14*, 100753.

(8) Ševčík, R.; Vaněk, J.; Michalicová, R.; Lubal, P.; Hermann, P.;
Santos, I. C.; Santos, I.; Campello, M. P. C. Formation and
Decomplexation Kinetics of Copper(II) Complexes with Cyclen
Derivatives Having Mixed Carboxylate and Phosphonate Pendant
Arms. *Dalton Trans.* **2016**, *45*, 12723−12733.

(9) Paúrová, M.; Havlíčková, J.; Pospíšilová, A.; Vetrík, M.; Císařová,
I.; Stephan, H.; Pietzsch, H.-J.; Hrubý, M.; Hermann, P.; Kotek, J.
Bifunctional Cyclam-Based Ligands with Phosphorus Acid Pendant
Moieties for Radiocopper Separation: Thermodynamic and Kinetic
Studies. *Chem. - Eur. J.* **2015**, *21*, 4671−4687.

(10) Martell, A. E.; Hancock, R. D. *Metal Complexes in Aqueous
Solutions*; Fackler, J. P., Ed.; Plenum Press: New York, 1996.

(11) McClung, M.; Harris, S. T.; Miller, P. D.; Bauer, D. C.;
Davison, K. S.; Dian, L.; Hanley, D. A.; Kendler, D. L.; Yuen, C. K.;
Lewiecki, E. M. Bisphosphonate Therapy for Osteoporosis: Benefits,
Risks, and Drug Holiday. *Am. J. Med.* **2013**, *126*, 13−20.

(12) Pols, H. A. P.; Felsenberg, D.; Hanley, D. A.; Štepán, J.; Muñoz-
Torres, M.; Wilkin, T. J.; Qin-Sheng, G.; Galich, A. M.; Vandormael,
K.; Yates, A. J.; et al. Multinational, Placebo-Controlled, Randomized
Trial of the Effects of Alendronate on Bone Density and Fracture Risk
in Postmenopausal Women with Low Bone Mass: Results of the
FOSIT Study. *Osteoporosis Int.* **1999**, *9*, 461−468.

(13) Greenspan, S. L.; Schneider, D. L.; McClung, M. R.; Miller, P.
D.; Schnitzer, T. J.; Bonin, R.; Smith, M. E.; DeLucca, P.; Gormley, G.
J.; Melton, M. E. Alendronate Improves Bone Mineral Density in
Elderly Women with Osteoporosis Residing in Long-Term Care
Facilities. *Ann. Intern. Med.* **2002**, *136*, 742−746.

(14) Kolesnikov-Gauthier, H.; Lemoine, N.; Tresch-Bruneel, E.;
Olivier, A.; Oudoux, A.; Penel, N. Efficacy and Safety of [153]Sm-
EDTMP as Treatment of Painful Bone Metastasis: A Large Single-
Center Study. *Support. Care Cancer* **2018**, *26*, 751−758.

(15) Agarwal, K. K.; Singla, S.; Arora, G.; Bal, C. ^{177}Lu-EDTMP for
Palliation of Pain from Bone Metastases in Patients with Prostate and
Breast Cancer: A Phase II Study. *Eur. J. Nucl. Med. Mol. Imaging* **2015**,
42, 79−88.

(16) Zha, Z.; Wu, Z.; Choi, S. R.; Ploessl, K.; Smith, M.; Alexoff, D.;
Zhu, L.; Kung, H. F. A New [68Ga]Ga-HBED-CC-Bisphosphonate as
a Bone Imaging Agent. *Mol. Pharmaceutics* **2020**, *17*, 1674−1684.

(17) Vitha, T.; Kubicek, V.; Hermann, P.; Elst, L. V.; Muller, R. N.;
Kolar, Z. I.; Wolterbeek, H. T.; Breeman, W. A.P.; Lukes, I.; Peters, J.
A. Lanthanide(III) Complexes of Bis(Phosphonate) Monoamide
Analogues of DOTA: Bone-Seeking Agents for Imaging and Therapy.
J. Med. Chem. **2008**, *51*, 677−683.

(18) Ferdani, R.; Stigers, D. J.; Fiamengo, A. L.; Wei, L.; Li, B. T. Y.;
Golen, J. A.; Rheingold, A. L.; Weisman, G. R.; Wong, E. H.;
Anderson, C. J. Synthesis, Cu(II) Complexation, ^{64}Cu-Labeling and

Biological Evaluation of Cross-Bridged Cyclam Chelators with Phosphonate Pendant Arms. *Dalton Trans.* **2012**, *41*, 1938−1950.

(19) Šimeček, J.; Hermann, P.; Havlíčková, J.; Herdtweck, E.; Kapp, T. G.; Engelbogen, N.; Kessler, H.; Wester, H.-J.; Notni, J. A Cyclen-Based Tetraphosphine Chelator for the Preparation of Radiolabeled Tetrameric Bioconjugates. *Chem. - Eur. J.* **2013**, *19*, 7748−7757.

(20) Baranyai, Z.; Reich, D.; Vágner, A.; Weineisen, M.; Tóth, I.; Wester, H.-J.; Notni, J. A Shortcut to High-Affinity Ga-68 and Cu-64 Radiopharmaceuticals: One-Pot Click Chemistry Trimerisation on the TRAP Platform. *Dalton Trans.* **2015**, *44*, 11137−11146.

(21) Šimeček, J.; Zemek, O.; Hermann, P.; Wester, H.-J.; Notni, J. A Monoreactive Bifunctional Triazacyclononane Phosphinate Chelator with High Selectivity for Gallium-68. *ChemMedChem* **2012**, *7*, 1375−1378.

(22) David, T.; Hlinová, V.; Kubíček, V.; Bergmann, R.; Striese, F.; Berndt, N.; Szöllősi, D.; Kovács, T.; Máthé, D.; Bachmann, M.; et al. Improved Conjugation, 64-Cu Radiolabeling, in Vivo Stability, and Imaging Using Nonprotected Bifunctional Macrocyclic Ligands: Bis(Phosphinate) Cyclam (BPC) Chelators. *J. Med. Chem.* **2018**, *61*, 8774−8796.

(23) Notni, J.; Pohle, K.; Wester, H. J. Be Spoilt for Choice with Radiolabelled RGD Peptides: Preclinical Evaluation of ^{68}Ga-TRAP-(RGD)$_3$. *Nucl. Med. Biol.* **2013**, *40*, 33−41.

(24) Price, E. W.; Zeglis, B. M.; Cawthray, J. F.; Ramogida, C. F.; Ramos, N.; Lewis, J. S.; Adam, M. J.; Orvig, C. H$_4$Octapa-Trastuzumab: Versatile Acyclic Chelate System for ^{111}In and ^{177}Lu Imaging and Therapy. *J. Am. Chem. Soc.* **2013**, *135*, 12707−12721.

(25) Boros, E.; Ferreira, C. L.; Cawthray, J. F.; Price, E. W.; Patrick, B. O.; Wester, D. W.; Adam, M. J.; Orvig, C. Acyclic Chelate with Ideal Properties for ^{68}Ga PET Imaging Agent Elaboration. *J. Am. Chem. Soc.* **2010**, *132*, 15726−15733.

(26) Comba, P.; Jermilova, U.; Orvig, C.; Patrick, B. O.; Ramogida, C. F.; Rück, K.; Schneider, C.; Starke, M. Octadentate Picolinic Acid-Based Bispidine Ligand for Radiometal Ions. *Chem. - Eur. J.* **2017**, *23*, 15945−15956.

(27) Ramogida, C. F.; Boros, E.; Patrick, B. O.; Zeisler, S. K.; Kumlin, J.; Adam, M. J.; Schaffer, P.; Orvig, C. Evaluation of H$_2$CHXdedpa, H$_2$Dedpa- and H$_2$CHXdedpa-N,N′-Propyl-2-NI Ligands for ^{64}Cu(II) Radiopharmaceuticals. *Dalton Trans.* **2016**, *45*, 13082−13090.

(28) Li, L.; Jaraquemada-Peláez, M. de G.; Kuo, H.-T.; Merkens, H.; Choudhary, N.; Gitschtaler, K.; Jermilova, U.; Colpo, N.; Uribe-Munoz, C.; Radchenko, V.; et al. Functionally Versatile and Highly Stable Chelator for ^{111}In and ^{177}Lu: Proof-of-Principle Prostate-Specific Membrane Antigen Targeting. *Bioconjugate Chem.* **2019**, *30*, 1539−1553.

(29) Spreckelmeyer, S.; Ramogida, C. F.; Rousseau, J.; Arane, K.; Bratanovic, I.; Colpo, N.; Jermilova, U.; Dias, G. M.; Dude, I.; Jaraquemada-Peláez, M. de G.; et al. P-NO$_2$−Bn−H$_4$Neunpa and H$_4$Neunpa−Trastuzumab: Bifunctional Chelator for Radiometalpharmaceuticals and ^{111}In Immuno-Single Photon Emission Computed Tomography Imaging. *Bioconjugate Chem.* **2017**, *28*, 2145−2159.

(30) Thiele, N. A.; Brown, V.; Kelly, J. M.; Amor-Coarasa, A.; Jermilova, U.; MacMillan, S. N.; Nikolopoulou, A.; Ponnala, S.; Ramogida, C. F.; Robertson, A. K. H.; et al. An Eighteen-Membered Macrocyclic Ligand for Actinium-225 Targeted Alpha Therapy. *Angew. Chem., Int. Ed.* **2017**, *56*, 14712−14717.

(31) Balogh, E.; Mato-Iglesias, M.; Platas-Iglesias, C.; Tóth, É.; Djanashvili, K.; Peters, J. A.; de Blas, A.; Rodríguez-Blas, T. Pyridine- and Phosphonate-Containing Ligands for Stable Ln Complexation. Extremely Fast Water Exchange on the Gd III Chelates. *Inorg. Chem.* **2006**, *45*, 8719−8728.

(32) Price, E. W.; Zeglis, B. M.; Lewis, J. S.; Adam, M. J.; Orvig, C. H$_6$Phospa-Trastuzumab: Bifunctional Methylenephosphonate-Based Chelator with ^{89}Zr, ^{111}In and ^{177}Lu. *Dalton Trans.* **2014**, *43*, 119−131.

(33) Kostelnik, T. I.; Wang, X.; Southcott, L.; Wagner, H. K.; Kubeil, M.; Stephan, H.; Jaraquemada-Peláez, M. de G.; Orvig, C. Rapid Thermodynamically Stable Complex Formation of [$^{Nat/111}$In]In^{3+},

[$^{Nat/90}$Y]Y^{3+}, and [$^{Nat/177}$Lu]Lu^{3+} with H$_6$Dappa. *Inorg. Chem.* **2020**, *59*, 7238−7251.

(34) Weekes, D. M.; Ramogida, C. F.; Jaraquemada-Peláez, M. de G.; Patrick, B. O.; Apte, C.; Kostelnik, T. I.; Cawthray, J. F.; Murphy, L.; Orvig, C. Dipicolinate Complexes of Gallium(III) and Lanthanum(III). *Inorg. Chem.* **2016**, *55*, 12544−12558.

(35) Jaraquemada-Peláez, M. de G.; Wang, X.; Clough, T. J.; Cao, Y.; Choudhary, N.; Emler, K.; Patrick, B. O.; Orvig, C. H$_4$Octapa: Synthesis, Solution Equilibria and Complexes with Useful Radiopharmaceutical Metal Ions. *Dalton Trans.* **2017**, *46*, 14647−14658.

(36) Abada, S.; Lecointre, A.; Christine, C.; Ehret-Sabatier, L.; Saupe, F.; Orend, G.; Brasse, D.; Ouadi, A.; Hussenet, T.; Laquerrière, P.; et al. Phosphonated Chelates for Nuclear Imaging. *Org. Biomol. Chem.* **2014**, *12*, 9601−9620.

(37) Shannon, R. D. Revised Effective Ionic Radii and Systematic Studies of Interatomic Distances in Halides and Chalcogenides. *Acta Crystallogr., Sect. A: Cryst. Phys., Diffr., Theor. Gen. Crystallogr.* **1976**, *32*, 751−767.

(38) Price, E. W.; Cawthray, J. F.; Bailey, G. A.; Ferreira, C. L.; Boros, E.; Adam, M. J.; Orvig, C. H$_4$Octapa: An Acyclic Chelator for ^{111}In Radiopharmaceuticals. *J. Am. Chem. Soc.* **2012**, *134*, 8670−8683.

(39) Price, E. W.; Cawthray, J. F.; Adam, M. J.; Orvig, C. Modular Syntheses of H$_4$Octapa and H$_2$Dedpa, and Yttrium Coordination Chemistry Relevant to ^{86}Y/^{90}Y Radiopharmaceuticals. *Dalton Trans.* **2014**, *43*, 7176−7190.

(40) Ramogida, C. F.; Cawthray, J. F.; Boros, E.; Ferreira, C. L.; Patrick, B. O.; Adam, M. J.; Orvig, C. H$_2$CHXdedpa and H$_4$CHX Octapa—Chiral Acyclic Chelating Ligands for ^{67,68}Ga and ^{111}In Radiopharmaceuticals. *Inorg. Chem.* **2015**, *54*, 2017−2031.

(41) Price, E. W.; Zeglis, B. M.; Cawthray, J. F.; Lewis, J. S.; Adam, M. J.; Orvig, C. What a Difference a Carbon Makes: H4octapa vs H4C3octapa, Ligands for In-111 and Lu-177 Radiochemistry. *Inorg. Chem.* **2014**, *53*, 10412−10431.

(42) Li, L.; Jaraquemada-Peláez, M. de G.; Aluicio-Sarduy, E.; Wang, X.; Jiang, D.; Sakheie, M.; Kuo, H.-T.; Barnhart, T. E.; Cai, W.; Radchenko, V.; et al. [$^{Nat/44}$Sc(Pypa)]$^-$: Thermodynamic Stability, Radiolabeling, and Biodistribution of a Prostate-Specific-Membrane-Antigen-Targeting Conjugate. *Inorg. Chem.* **2020**, *59*, 1985−1995.

(43) Frassineti, C.; Ghelli, S.; Gans, P.; Sabatini, A.; Moruzzi, M. S.; Vacca, A. Nuclear Magnetic Resonance as a Tool for Determining Protonation Constants of Natural Polyprotic Bases in Solution. *Anal. Biochem.* **1995**, *231*, 374−382.

(44) Gans, P.; Sabatini, A.; Vacca, A. Determination of Equilibrium Constants from Spectrophotometric Data Obtained from Solutions of Known PH: The Program PHab. *Ann. Chim.* **1999**, *89*, 45−49.

(45) Gans, P.; Sabatini, A.; Vacca, A. Investigation of Equilibria in Solution. Determination of Equilibrium Constants with the HYPER-QUAD Suite of Programs. *Talanta* **1996**, *43*, 1739−1753.

(46) Alderighi, L.; Gans, P.; Ienco, A.; Peters, D.; Sabatini, A.; Vacca, A. Hyperquad Simulation and Speciation (HySS): A Utility Program for the Investigation of Equilibria Involving Soluble and Partially Soluble Species. *Coord. Chem. Rev.* **1999**, *184*, 311−318.

(47) Harris, W. R.; Carrano, C. J.; Raymond, K. N. Spectrophotometric Determination of the Proton-Dependent Stability Constant of Ferric Enterobactin. *J. Am. Chem. Soc.* **1979**, *101*, 2213−2214.

(48) Casabianca, L. B. Calculating Nuclear Magnetic Resonance Chemical Shifts in Solvated Systems. *Magn. Reson. Chem.* **2020**, *58*, 611−624.

(49) Krivdin, L. B. Computational ^{1}H NMR: Part 1. Theoretical Background. *Magn. Reson. Chem.* **2019**, *57*, 897−914.

(50) Krivdin, L. B. Computational ^{1}H NMR: Part 2. Chemical Applications. *Magn. Reson. Chem.* **2020**, *58*, 5−14.

(51) Toomsalu, E.; Burk, P. Critical Test of Some Computational Methods for Prediction of NMR ^{1}H and ^{13}C Chemical Shifts. *J. Mol. Model.* **2015**, *21*, 1−21.

(52) Adamo, C.; Barone, V. Toward Reliable Density Functional Methods without Adjustable Parameters: The PBE0Model. *J. Chem. Phys.* **1999**, *110*, 6158−6170.

(53) Jensen, F. Segmented Contracted Basis Sets Optimized for Nuclear Magnetic Shielding. *J. Chem. Theory Comput.* **2015**, *11*, 132−138.

(54) Bagno, A.; D'Amico, F.; Saielli, G. Computing the 1H NMR Spectrum of a Bulk Ionic Liquid from Snapshots of Car-Parrinello Molecular Dynamics Simulations. *ChemPhysChem* **2007**, *8*, 873−881.

(55) Dračínský, M.; Bouř, P.; Hodgkinson, P. Temperature Dependence of NMR Parameters Calculated from Path Integral Molecular Dynamics Simulations. *J. Chem. Theory Comput.* **2016**, *12*, 968−973.

(56) de Dios, A. C.; Jameson, C. J. Recent Advances in Nuclear Shielding Calculations. *Annu. Rep. NMR Spectrosc.* **2012**, *77*, 1−80.

(57) Gutten, O.; Rulíšek, L. Predicting the Stability Constants of Metal-Ion Complexes from First Principles. *Inorg. Chem.* **2013**, *52*, 10347−10355.

(58) Roy, L. E.; Martin, L. R. Theoretical Prediction of Coordination Environments and Stability Constants of Lanthanum Lactate Complexes in Solution. *Dalton Trans.* **2016**, *45*, 15517−15522.

(59) Rodríguez-Rodríguez, A.; Regueiro-Figueroa, M.; Esteban-Gómez, D.; Tripier, R.; Tircsó, G.; Kálmán, F. K.; Bényei, A. C.; Tóth, I.; Blas, A. De; Rodríguez-Blas, T.; et al. Complexation of Ln^{3+} Ions with Cyclam Dipicolinates: A Small Bridge That Makes Huge Differences in Structure, Equilibrium, and Kinetic Properties. *Inorg. Chem.* **2016**, *55*, 2227−2239.

(60) Le Fur, M.; Molnár, E.; Beyler, M.; Fougère, O.; Esteban-Gómez, D.; Rousseaux, O.; Tripier, R.; Tircsó, G.; Platas-Iglesias, C. Expanding the Family of Pyclen-Based Ligands Bearing Pendant Picolinate Arms for Lanthanide Complexation. *Inorg. Chem.* **2018**, *57*, 6932−6945.

(61) Kálmán, F. K.; Végh, A.; Regueiro-Figueroa, M.; Tóth, É.; Platas-Iglesias, C.; Tircsó, G. H₄Octapa: Highly Stable Complexation of Lanthanide(III) Ions and Copper(II). *Inorg. Chem.* **2015**, *54*, 2345−2356.

(62) Holland, J. P. Predicting the Thermodynamic Stability of Zirconium Radiotracers. *Inorg. Chem.* **2020**, *59*, 2070−2082.

(63) Ochterski, J. W. *Thermochemistry in Gaussian*; Gaussian Inc: Pittsburgh PA, 2000. Online at https://gaussian.com/thermo/

(64) Zeng, X.; Coquière, D.; Alenda, A.; Garrier, E.; Prangé, T.; Li, Y.; Reinaud, O.; Jabin, I. Efficient Synthesis of Calix[6]Tmpa: A New Calix[6]Azacryptand with Unique Conformational and Host−Guest Properties. *Chem. - Eur. J.* **2006**, *12*, 6393−6402.

(65) Sheldrick, G. M. Crystal Structure Refinement with SHELXL. *Acta Crystallogr., Sect. C: Struct. Chem.* **2015**, *71*, 3−8.

(66) Dolomanov, O. V.; Bourhis, L. J.; Gildea, R. J.; Howard, J. A. K.; Puschmann, H. OLEX2: A Complete Structure Solution, Refinement and Analysis Program. *J. Appl. Crystallogr.* **2009**, *42*, 339−341.

(67) Paoletti, P.; Fabbrizzi, L.; Barbucci, R. Thermochemistry of Metal-Polyamine Complexes. *Inorg. Chim. Acta, Rev.* **1973**, *7*, 43−68.

(68) Gran, G. Determination of the Equivalence Point in Potentiometric Titrations. Part II. *Analyst* **1952**, *77*, 661−671.

(69) Paul, M. A.; Long, F. A. H0 And Related Indicator Acidity Function. *Chem. Rev.* **1957**, *57*, 1−45.

(70) Baes, C. F. J.; Mesmer, R. E. *The Hydrolysis of Cations*; Wiley-Interscience: New York, 1976.

(71) Frisch, M. J.; Trucks, G. W.; Schlegel, H. B.; Scuseria, G. E.; Robb, M. A.; Cheeseman, J. R.; Scalmani, G.; Barone, V.; Petersson, G. A.; Nakatsuji, H.; et al. *Gaussian 16*, rev. C.01; Gaussian, Inc.: Wallingford, CT, 2016.

(72) Li, X.; Frisch, M. J. Energy-Represented Direct Inversion in the Iterative Subspace within a Hybrid Geometry Optimization Method. *J. Chem. Theory Comput.* **2006**, *2*, 835−839.

(73) Grimme, S.; Ehrlich, S.; Goerigk, L. Effect of the Damping Function in Dispersion Corrected Density Functional Theory. *J. Comput. Chem.* **2011**, *32*, 1456−1465.

(74) Grimme, S.; Antony, J.; Ehrlich, S.; Krieg, H. A Consistent and Accurate Ab Initio Parametrization of Density Functional Dispersion Correction (DFT-D) for the 94 Elements H-Pu. *J. Chem. Phys.* **2010**, *132*, 154104.

(75) Smith, D. G. A.; Burns, L. A.; Patkowski, K.; Sherrill, C. D. Revised Damping Parameters for the D3 Dispersion Correction to Density Functional Theory. *J. Phys. Chem. Lett.* **2016**, *7*, 2197−2203.

(76) Weigend, F.; Ahlrichs, R. Balanced Basis Sets of Split Valence, Triple Zeta Valence and Quadruple Zeta Valence Quality for H to Rn: Design and Assessment of Accuracy. *Phys. Chem. Chem. Phys.* **2005**, *7*, 3297−3305.

(77) Martin, J. M. L.; Sundermann, A. Correlation Consistent Valence Basis Sets for Use with the Stuttgart-Dresden-Bonn Relativistic Effective Core Potentials: The Atoms Ga-Kr and In-Xe. *J. Chem. Phys.* **2001**, *114*, 3408−3420.

(78) Dolg, M.; Wedig, U.; Stoll, H.; Preuss, H. Energy-adjusted Ab Initio Pseudopotentials for the First Row Transition Elements. *J. Chem. Phys.* **1987**, *86*, 866−872.

(79) Cao, X.; Dolg, M. Valence Basis Sets for Relativistic Energy-Consistent Small-Core Lanthanide Pseudopotentials. *J. Chem. Phys.* **2001**, *115*, 7348−7355.

(80) Cao, X.; Dolg, M. Segmented Contraction Scheme for Small-Core Lanthanide Pseudopotential Basis Sets. *J. Mol. Struct.: THEOCHEM* **2002**, *581*, 139−147.

(81) Schuchardt, K. L.; Didier, B. T.; Elsethagen, T.; Sun, L.; Gurumoorthi, V.; Chase, J.; Li, J.; Windus, T. L. Basis Set Exchange: A Community Database for Computational Sciences. *J. Chem. Inf. Model.* **2007**, *47*, 1045−1052.

(82) Pritchard, B. P.; Altarawy, D.; Didier, B.; Gibson, T. D.; Windus, T. L. New Basis Set Exchange: An Open, Up-to-Date Resource for the Molecular Sciences Community. *J. Chem. Inf. Model.* **2019**, *59*, 4814−4820.

(83) Feller, D. The Role of Databases in Support of Computational Chemistry Calculations. *J. Comput. Chem.* **1996**, *17*, 1571−1586.

(84) Vícha, J.; Patzschke, M.; Marek, R. A Relativistic DFT Methodology for Calculating the Structures and NMR Chemical Shifts of Octahedral Platinum and Iridium Complexes. *Phys. Chem. Chem. Phys.* **2013**, *15*, 7740−7754.

(85) Bühl, M.; Reimann, C.; Pantazis, D. A.; Bredow, T.; Neese, F. Geometries of Third-Row Transition-Metal Complexes from Density-Functional Theory. *J. Chem. Theory Comput.* **2008**, *4*, 1449−1459.

(86) Vícha, J.; Novotný, J.; Straka, M.; Repisky, M.; Ruud, K.; Komorovsky, S.; Marek, R. Structure, Solvent, and Relativistic Effects on the NMR Chemical Shifts in Square-Planar Transition-Metal Complexes: Assessment of DFT Approaches. *Phys. Chem. Chem. Phys.* **2015**, *17*, 24944−24955.

(87) Quintal, M. M.; Karton, A.; Iron, M. A.; Boese, A. D.; Martin, J. M. L. Benchmark Study of DFT Functionals for Late-Transition-Metal Reactions. *J. Phys. Chem. A* **2006**, *110*, 709−716.

(88) Dohm, S.; Hansen, A.; Steinmetz, M.; Grimme, S.; Checinski, M. P. Comprehensive Thermochemical Benchmark Set of Realistic Closed-Shell Metal Organic Reactions. *J. Chem. Theory Comput.* **2018**, *14*, 2596−2608.

(89) Kirschner, K. N.; Reith, D.; Heiden, W. The Performance of Dunning, Jensen, and Karlsruhe Basis Sets on Computing Relative Energies and Geometries. *Soft Mater.* **2020**, *18*, 200−214.

(90) Bauzá, A.; Quiñonero, D.; Deya, P. M.; Frontera, A. Is the Use of Diffuse Functions Essential for the Properly Description of Noncovalent Interactions Involving Anions? *J. Phys. Chem. A* **2013**, *117*, 2651−2655.

(91) Martinez, L.; Andrade, R.; Birgin, E. G.; Martinez, J. M. PACKMOL: A Package for Building Initial Configurations for Molecular Dynamics Simulations. *J. Comput. Chem.* **2009**, *30*, 2157−2164.

(92) Cheeseman, J. R.; Trucks, G. W.; Keith, T. A.; Frisch, M. J. A Comparison of Models for Calculating Nuclear Magnetic Resonance Shielding Tensors. *J. Chem. Phys.* **1996**, *104*, 5497−5509.

(93) Wolinski, K.; Hinton, J. F.; Pulay, P. Efficient Implementation of the Gauge-Independent Atomic Orbital Method for NMR Chemical Shift Calculations. *J. Am. Chem. Soc.* **1990**, *112*, 8251−8260.

(94) Pawlak, T.; Niedzielska, D.; Vícha, J.; Marek, R.; Pazderski, L. Dimeric Pd(II) and Pt(II) Chloride Organometallics with 2-Phenylpyridine and Their Solvolysis in Dimethylsulfoxide. *J. Organomet. Chem.* **2014**, *759*, 58−66.

(95) Reid, D. M.; Kobayashi, R.; Collins, M. A. Systematic Study of Locally Dense Basis Sets for NMR Shielding Constants. *J. Chem. Theory Comput.* **2014**, *10*, 146−152.

(96) Jensen, F. Unifying General and Segmented Contracted Basis Sets. Segmented Polarization Consistent Basis Sets. *J. Chem. Theory Comput.* **2014**, *10*, 1074−1085.

(97) Dennington, R.; Keith, T. A.; Millam, J. M. *GaussView,* ver. 6.0.16; Semichem Inc.: Shawnee Mission, KS, 2016.